Numerical investigation of interaction between anticyclonic eddy and semidiurnal internal tide in the northeastern South China Sea

Liming Fan[1], Hui Sun[1*], Qingxuan Yang[1,2*], Jianing Li[1]

[1]Frontier Science Center for Deep Ocean Multispheres and Earth System (FDOMES) and Physical Oceanography Laboratory/Sanya Oceanographic Institution, Ocean University of China, Qingdao/Sanya, 266100/572024, China
[2]Laoshan Laboratory, Qingdao, 266100, China

Correspondence to: Hui Sun (sunhui@ouc.edu.cn), Qingxuan Yang(yangqx@ouc.edu.cn)

Abstract. We investigate the interaction between an anticyclonic eddy (AE) and semidiurnal internal tide (SIT) on the continental slope of the northeastern South China Sea (SCS), using a high spatiotemporal resolution numerical model. Two key findings are as follows. First, the AE promotes energy conversion from low-mode to higher-mode SIT; additionally, production terms indicate that energy is also transferred from the SIT field to the eddy field at an average rate of 3.0 mW m^{-2} (accounting for 7% of the incoming energy flux of SIT when integrated over the eddy diameter). Second, the AE can modify the spatial distribution of tidal-induced dissipation by refracting, scattering, and reflecting low-mode SIT. The phase and group velocities of the SIT are significantly influenced by the eddy field, resulting in a northward or southward shift of the internal tidal rays. These findings deepen our understanding of the complex interactions between AE and SIT, as well as their impacts on energy conversion, wave propagation, and coastal processes.

1 Introduction

In the ocean, mesoscale dynamic processes (50–300 km) play a transitional role in the energy cascade; among them, internal tide (IT) and mesoscale eddy (ME) are two of the most ubiquitous processes (Chelton et al., 2011; Müller et al., 2012; Faghmous et al., 2015; Zhao et al., 2016). The former is generated by the interaction of barotropic tide (BT) and topography in a stratified ocean, deriving about 1 TW energy from BT globally (Egbert and Ray, 2003). The latter is often generated by hydrodynamic instabilities of background currents (Zhang et al., 2016), and accounts for about 80% of the total oceanic kinetic energy (Ferrari and Wunsch, 2009). Moreover, both IT and ME have essential effects on deep-ocean mixing, heat and mass transports, ecological productivity (Munk and Wunsch, 1998; Wunsch, 1999; Da Silva et al., 2002; McGillicuddy et al., 2007; Stastna and Lamb, 2008; Sharples et al., 2009; Lermusiaux et al., 2010; Duda et al., 2014; Zhang et al., 2014).

The propagation and dissipation processes of ITs and MEs have been research foci in recent years. When the IT obtains energy from the large-scale BT, its low-mode part undergoes long-distance propagation (exceeding 1000 km) to redistribute the energy (Zhao, 2017; Alford et al., 2019). During the propagation, the low-mode IT is susceptible to the states of background

fields, leading to incoherence and nonstationarity (Savage et al., 2020). The high-mode IT, on the contrary, dissipates mainly near the generation site due to its short wavelength and large vertical shear (Vic et al., 2019). Eventually, the IT-induced mixing will affect the spatiotemporal variability of oceanic meridional overturning circulation (Munk and Wunsch, 1998). Unlike ITs, MEs have significant impacts on the meridional transport of mass and zonal transport of heat during their

35   propagations (Wunsch et al., 1999; Zhang et al., 2014). In addition, the dissipation of MEs is linked to sub-mesoscale processes (Zhang et al., 2016; Yang et al., 2019; Liu et al., 2022).

Due to the comparable horizontal scales of low-mode IT and ME, their interaction occurs easily and becomes a hotspot for studying multiscale dynamical motions (interaction process involves multi-modal/multiscale internal tides). When the interaction occurs, IT can transfer energy to ME, causing mesoscale kinetic energy to alter (Barkan et al., 2017, 2021). For

40   example, in the Southern Ocean, the eddy field receives 2.2±0.6 mW m^{-2} energy from the internal wave (IW) field (with frequencies ranging from f to N and including tidal frequencies) through vertical shear (Cusack et al., 2020). Furthermore, and most notably, MEs can modulate the generation, propagation, and inter-modal energy redistribution of ITs. Because the ME has a significantly longer time scale than the IT, it is common to assume the ME as the background field and then focus on the modulation of the IT by the ME when studying their interaction.

45   Regarding how ME affects the generation of IT, studies have shown that the interaction between BT and baroclinic eddy field can generate internal waves (Krauss, 1999), which are most efficiently generated when their horizontal scales are comparable (Lelong and Kunze, 2013). ME mostly modulates the propagation of IT in terms of refraction and scattering. IT is refracted as it passes through the ME field (which corresponds to a non-uniform propagation medium), thus changing its propagation direction (Huang et al., 2018; Guo et al., 2023). Meanwhile, IT can scatter from mode 1 to mode 2 and higher

50   modes, accompanied by an inter-modal redistribution of IT energy (Dunphy and Lamb, 2014; Clément et al., 2016; Dunphy et al., 2017; Wang et al., 2023).

The refraction and scattering of IT can be detected in in-situ observations (Huang et al., 2018; Löb et al., 2020). However, there are some geographic scale restrictions when using observed data. So, numerical simulation of the whole process of IT propagation is an essential way to study interaction between IT and ME. Using numerical models, researchers have directly

55   simulated interaction processes (Dunphy and Lamb, 2014; Zaron and Egbert, 2014). To examine the energy changes during the interaction more accurately, Kelly and Lermusiaux (2016) proposed a refined IT energy equation to quantify the effect of background flow on internal wave generation and propagation. This equation has been used in the Middle Atlantic Bight and Palau Island waters (Pan et al., 2021), suggesting that it is an effective tool to study the interaction.

The SCS is a large marginal sea in the western Pacific Ocean, where IT and ME are ubiquitous; they are particularly energetic

60   in the northern SCS (Niwa and Hibiya, 2004; Jan et al., 2008; Cheng et al., 2009; Chen et al., 2011; Guo et al., 2012; Li et al., 2012; Lin et al., 2015; Zhang et al., 2016; Cao et al., 2017). The northern SCS is therefore an excellent area for investigating the interaction between IT and ME. Such knowledge of the interaction between IT and background flow (e.g., ME) will conduce to a better understanding of the energy budget among different dynamic processes in the study area. Such a study can also provide a reference for improving IT prediction and developing more reliable coupled ocean-climate models.

65   The remainder of this paper is organized as follows. In section 2, we provide an introduction to the dataset used and the energy equation of IT. Section 3 is divided into two parts: the first part examines the interaction between anticyclonic eddy (AE) and semidiurnal internal tide (SIT) from a dynamic and energetic perspective, and the second explores the impact of AE on the kinematic characteristics of SIT. Contributions of interaction terms to SIT energy are discussed in section 4, followed by conclusions in section 5.

2 Data and methods

2.1 Data

We use the MIT general circulation model (MITgcm) LLC4320 outputs (Marshall et al., 1997). The model has a horizontal resolution of 1/48° (about 2 km at the equator) and 90 vertical layers (with a vertical resolution of about 1 m at the surface and 30 m down to 500 m). The fine grid allows for more accurate characterization of topographic changes, which directly affect the generation of IT (Niwa and Hibiya, 2004; Kelly et al., 2021). Note that LLC4320 uses a global-scale LLC (Lat-Lon-Cap) grid, so it does not need open boundaries (Menemenlis et al., 2021). The model can effectively simulate free-propagating internal waves such as ITs, while general regional models get weaker IWs in the simulated region when they do not introduce forcing of low-mode IWs from the external region (unless a multi-layer nesting strategy is adopted) (Liu and Gan, 2016; Mazloff et al., 2020). The outputs are from a forward simulation without any artificial intervention such as data assimilation, so it is reliable for diagnosing the energy equation (Cummings and Smedstad, 2013). In addition, LLC4320 has been widely used to analyse basin-scale circulations, internal waves, and mesoscale and sub-mesoscale processes (Rocha et al., 2016; Lin et al., 2020; Su et al., 2020; Goldsworth et al., 2021; Liu et al., 2023; Zhang et al., 2023). Despite these advantages, LLC4320 has some shortcomings. It does not consider near-bottom drag and dissipation of BT, resulting in the simulated IT being slightly stronger than the observed (Yu et al., 2019; Buijsman et al., 2020). This weakness does not undermine the conclusions of this research, because we focus on investigating the mechanisms of interaction between AE and SIT, rather than comparing with field observations.

2.2 Methods

By introducing background flow and modal decomposition, the tidal-averaged and depth-integrated energy equation of mode-n IT is given as follows (Kelly and Lermusiaux, 2016a):

$$\nabla \cdot \langle \boldsymbol{F}_n \rangle + \sum_{m=0}^{\infty} \langle A_{mn} \rangle = \sum_{m=0}^{\infty} \langle C_{mn} \rangle + \sum_{m=0}^{\infty} \langle P_{mn}^S + P_{mn}^B \rangle + \langle D_n \rangle , \tag{1}$$

where $\langle \cdot \rangle$ denotes the average over several tidal cycles (62 h is used in this paper), and ∇ denotes horizontal divergence. $\boldsymbol{F}_n$, A_{mn}, C_{mn}, P_{mn}^S, P_{mn}^B, and D_n are the mode-n IT energy flux, advection by the background flow, topographic conversion, shear production, and horizontal buoyancy production, and dissipation terms, respectively. A detailed introduction to calculation for each term is given in Appendix A. Eq. (1) includes interaction terms between background flow and IT. One of the terms is the

95   advection term ($\langle A_{mn} \rangle$), which characterizes the influence of background flow on IT propagation, but does not involve any energy transfer between them. Another term is the production ($\langle P_{mn}^S + P_{mn}^B \rangle$), which measures the exchanged energy between background flow and IT. Noted that the advection, conversion ($\langle C_{mn} \rangle$), and production terms all involve cross-modal exchange terms between modes m and n, indicating inter-modal energy scattering. Besides, the energy dissipation term ($\langle D_n \rangle$) includes nonlinear wave-wave interactions (e.g., parametric subharmonic instability process), self-advection, and numerical errors

100 (Appendix B verifies the reasonableness of the dissipation term). The equation separates different modes to better evaluate changes in each IT mode, and explores scattering between different modes.

Note that Eq. (1) needs to satisfy the assumption of small-amplitude linear internal waves (Kelly and Lermusiaux, 2016a). We find that the Froude number ($F_r = U_0/c$, where U_0 is BT tidal current, and c is phase speed) of the first three modes of SITs in the study area is much less than 1 (not shown), which means that the first three modes of SITs are applicable to Eq.

105 (1).

Before using Eq. (1) for energy analysis, we need to extract ME and IT from the LLC4320 data. In this paper, the background flow (including MEs) is obtained by time averaging the LLC4320 data over 62 h; and the semi-diurnal signal is extracted using a 4th-order Butterworth filter method with the bandpass band of 1.73-2.13 cpd (cycles per day). Then, the baroclinic velocity of SIT is obtained by subtracting the depth average from the filtering results. For the calculation of pressure perturbation,

110 readers are referred to Wang et al. (2016). To reduce the computational load, we select a grid resolution of 1/24° (half of the original resolution) for our calculation, because although the horizontal wavelength of the IT is inversely related to the mode number (based on the dispersion relation of linear IWs, $\lambda_h = \sqrt{(N^2 - \omega^2)/(\omega^2 - f^2)}\,\lambda_z$), the resolution of 1/24° is fine enough to distinguish the first five modes of SITs in the tropical zone (Buijsman et al., 2020).

3 Results

115 The study area of the northeastern SCS is shown in Fig. 1a. We selected a period for analysis, corresponding to 131-170 days. During this period, an active AE appeared on the western side of the Luzon Strait (LS), which passed through the continental slope of the northeastern SCS (region R2 in Fig. 1a), and eventually dissipated nearshore (region R2 in Fig. 1a). Both Fig. 1b and Fig. 1c show three spring tide moments during this period, although the zonal semidiurnal barotropic tidal current from LLC4320 is slightly greater than that from TPXO-v9 (Egbert and Erofeeva, 2002), which is consistent with the conclusion of

120 Yu et al. (2019). The slight difference between the spring tide moments in Fig. 1b-c may be due to the bandpass filtering, so we use the TPXO-v9 result to determine the spring tide moments, which occurred on days 134, 150, and 162, respectively. In Fig. 1b, we notice the phenomenon of tidal inequality, which may be related to the model's use of celestial gravitational tidal force, but it is not focused on due to the small influence on the semidiurnal BT.
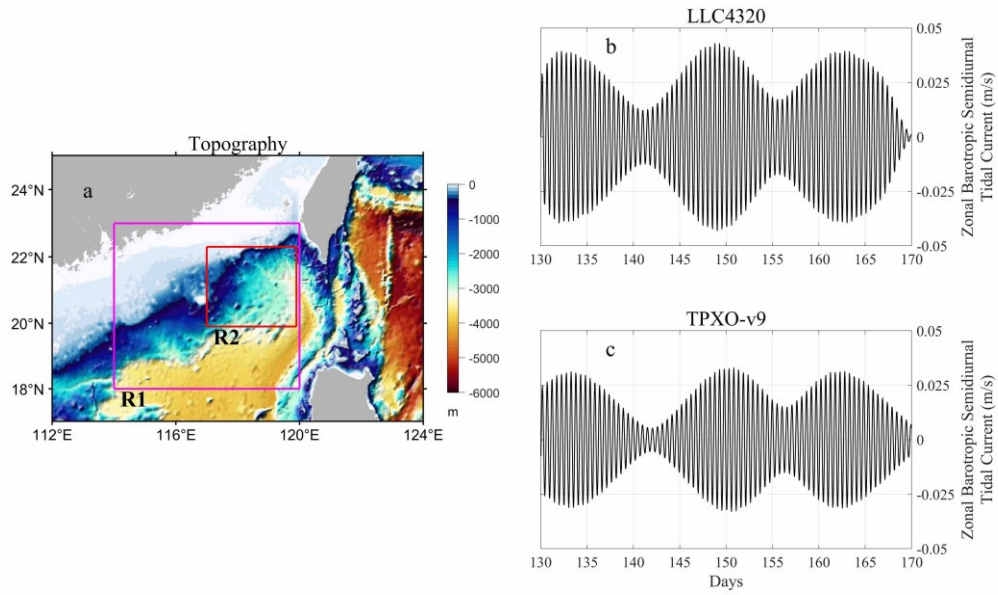
Figure 1. (a) Topographic distribution of the northern SCS, where R1 is the study area (114-120° E, 18-23° N) and R2 is the impact area of the AE (117.0-119.9° E, 19.9-22.3° N). (b) and (c) are the regionally averaged semidiurnal BT currents in region R2 extracted from the MITgcm LLC4320 and TPXO-v9 datasets, respectively. Note that the phase velocity of the semidiurnal BT in region R2 is of the magnitude of 100 m s^{-1}, and the zonal distance of region R2 is about 300 km, implying that the phase change of BT in region R2 could be ignored.

To better clarify the propagation distance of the SIT, we calculated the energy fluxes for the first three modes of SITs throughout the whole SCS (at depths deeper than 200 m). Take day 151 as an example in Fig. 2. The propagation distance of mode-1 SIT exceeds 1000 km, which is consistent with the distance of Xu et al. (2016). The mode-2 SIT propagates about 400 km, and mode-3 SIT propagates about 80 km.
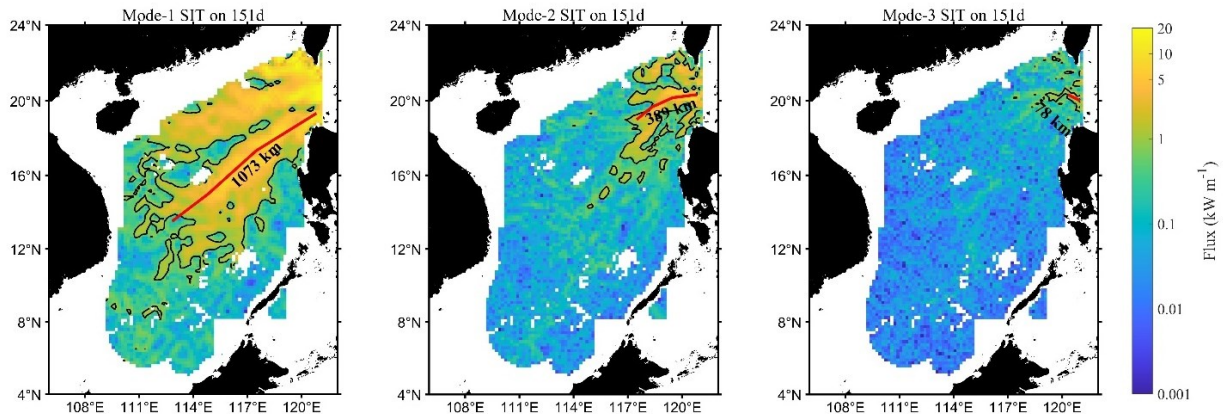
Figure 2. Spatial distribution of energy flux for the first three modes of SITs on day 151 in the SCS (in log scale), the red curves are the main propagation path of the first three modes of SITs, the black values indicate the propagation distance of the red curves.

3.1 Dynamics and energetics of the interaction between AE and SIT

To analyse the dynamics of the interaction between AE and the first three modes of SITs, we introduce the energy equation of IT containing the background flow, as presented in Eq. (1). Eq. (1) reveals that $\nabla \cdot \langle \boldsymbol{F}_n \rangle$ can reflect the increase or decrease of IT energy, with positive value indicating a local source and negative value indicating a local sink. The increase or decrease of IT energy is mainly determined by three factors: topographic conversion term ($\langle C_{mn} \rangle$), background flow advection term ($\langle A_{mn} \rangle$), and energy exchange term between background flow and IT ($\langle P_{mn}^S + P_{mn}^B \rangle$).

In the following analysis, we primarily focus on the relative changes during the three spring tide moments. Since later analyses (Fig. 3d, Fig. 4d, and Fig.5d) show that changes in IT energy lag slightly behind changes in BT, we focus on days 137, 151, and 164.

3.1.1 Changes in the energy of SIT during the interaction

First, we analyse the impact of AE and SIT interaction on SIT energy. Figure 3 shows that the total energy (TE, the sum of the depth-integrated horizontal kinetic energy (HKE) and available potential energy (APE)) of mode-1 SIT increases significantly during the AE period (days 146-162, which is determined through the change in area-integrated eddy kinetic energy), and decreases synchronously as the AE gradually dissipates on the continental slope (Fig. 3c). To quantify the energy input, we integrate the SIT energy flux on each side of region R2. The calculation shows that the energy input was 3.15 GW on day 137, increased to 4.31 GW on day 151, and then decreased to 3.27 GW on day 164, indicating an increase in SIT energy on day 151.

Figures 3d-f show that the energy of mode-1 SIT has three peaks (the peaks of SIT energy lag behind the spring tide moments by a few days because it takes time for the low-mode SITs to propagate from the generation source of the LS to R1 area) with a neap-spring tidal cycle. The neap-spring tidal cycle is influenced by the amplitudes of tidal constituents and the convergence or divergence of semidiurnal or diurnal tides, which are related to changes in the Moon's phase or declination (Kvale, 2006). According to Fig. 3d, the TE of mode-1 SIT increased by 27% from day 137 to day 151, and decreased by 11% from day 151 to day 164. The changes in HKE (Fig. 3e) and APE (Fig.3f) are similar to that of TE, with an overall rising and then declining trend. In addition, the HKE-to-APE ratio (r_E) of progressive internal waves obeys

$$r_E = \frac{\text{HKE}}{\text{APE}} = \frac{\omega^2 + f^2}{\omega^2 - f^2}, \tag{2}$$

where ω is the frequency of SIT and f is the local Coriolis frequency.

In Fig. 3f, the APE of mode-1 SIT in region R2 is consistent with the result of HKE/r_E, suggesting that the mode-1 SIT in the northeastern SCS satisfies the characteristic of free propagation (Zhao et al., 2010). We also compare the energy of mode-1 SIT with the results of Zhao and Qiu (2023), which verifies that the energy of mode-1 SIT in region R1 is larger in the north than in the south, and stronger in the east than in the west, suggesting that the LLC4320 data can simulate the generation and propagation of SIT properly.
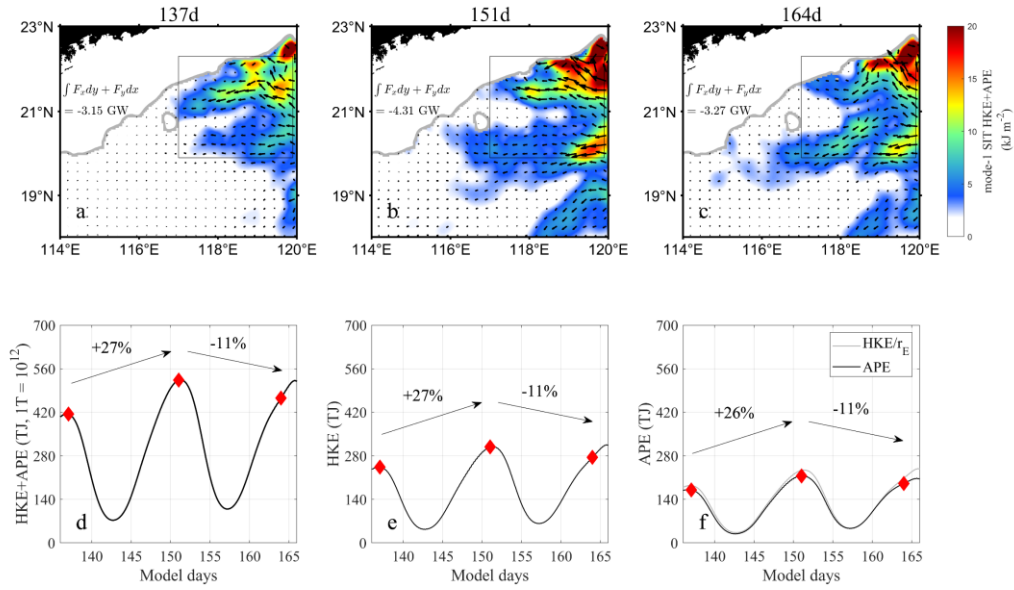
Figure 3. (a-c) Spatial distribution of mode-1 SIT energy on days 137, 151, and 164. Black arrows represent energy flux of SIT, and grey contours represent the depth of 250 m. **(d-f)** Time series of TE, HKE, and APE obtained from area integral over the region R2, with the red diamonds corresponding to days 137, 151, and 164, respectively. The grey curve in **(f)** is calculated using Eq. (2).

Figure 4 shows the energy of mode-2 SIT. The trend of increasing and then decreasing of TE is still evident, with a significant feature that the TE is concentrated around the AE (Fig. 4b). According to area integral over the region R2, there was 0.45 GW of energy input into the study area on day 137, which increased to 0.60 GW on day 151 before decreasing to 0.55 GW on day 164.

Figure 2 shows that mode-2 SIT can only propagate westward to 117°E, because higher-mode ITs are more prone to dissipation and cannot travel long distances (Nikurashin et al., 2011; Vic et al., 2019). Figure 4d indicates that the TE of mode-2 SIT first increased by 20% from day 137 to day 151, and then decreased by 10% from day 151 to day 164. Compared to changes in the TE of mode-1 SIT, the enhancement ratio is smaller, but the reduction ratio remains roughly the same. HKE and APE have almost the same temporal variation as TE (Fig. 4e-f). Note that in region R2, the calculated r_E is smaller than the theoretical r_E, with the most significant difference occurring during spring tide. This implies that refraction likely occurred for mode-2 SIT, leading to topographic reflection and deviation of calculated r_E from the theoretical value, as discussed in section 3.2 (Martini et al., 2007; Hamann et al., 2021).
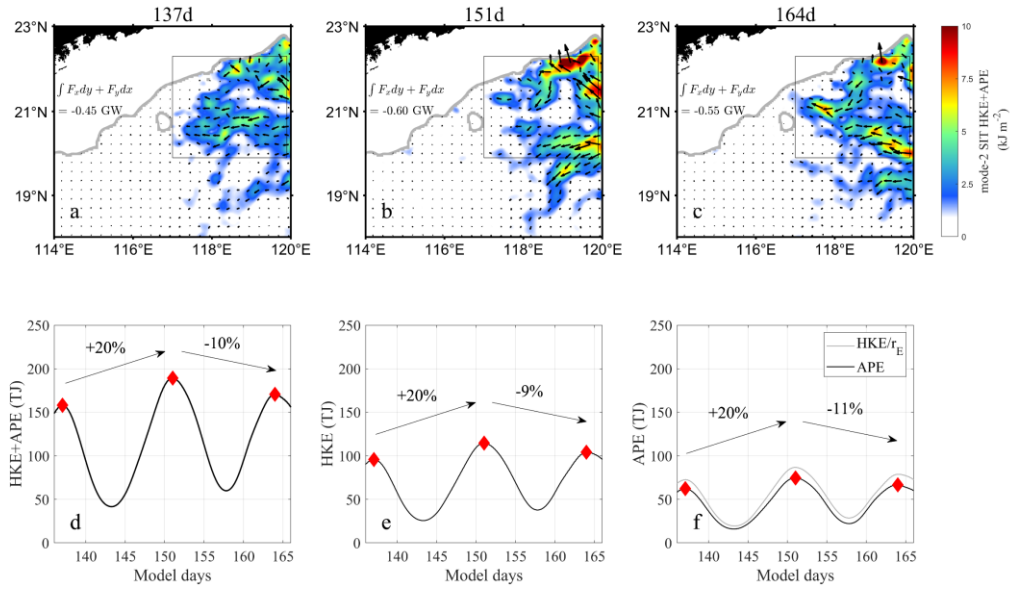
Figure 4. Same as Fig. 3, but for mode-2 SIT.

The energy of mode-3 SIT is shown in Fig. 5. The TE is not distributed in stripes or large patches as in the first two modes, but in dispersed small blocks, implying that the propagation distance of mode 3 is shorter than that of the first two modes. The horizontal scale of these small blocks is equivalent to the propagation distance of mode-3 SIT shown in Fig. 2 (roughly 80 km). From the integral of energy flux in region R2, there was 0.05 GW energy input into the study area on day 137, 0.01 GW on day 151, and 0.07 GW on day 164, with a trend of decreasing and then increasing, which is opposite to the first two modes. Figure 5d shows that the TE of mode-3 SIT has an increasing-then-decreasing trend (increased by 8% from day 137 to day 151 and decreased by 1% from day 151 to day 164), which is closer to the change in HKE (Fig. 5e) rather than to the change in APE (Fig. 5f). Differences in temporal trends of HKE and APE lead to significant variation between calculated r_E and theoretical r_E. In summary, there existed local generation sources for mode-3 SIT in region R2, since the TE of mode-3 SIT increased when the external energy input decreased on day 151 (only by 0.01 GW).
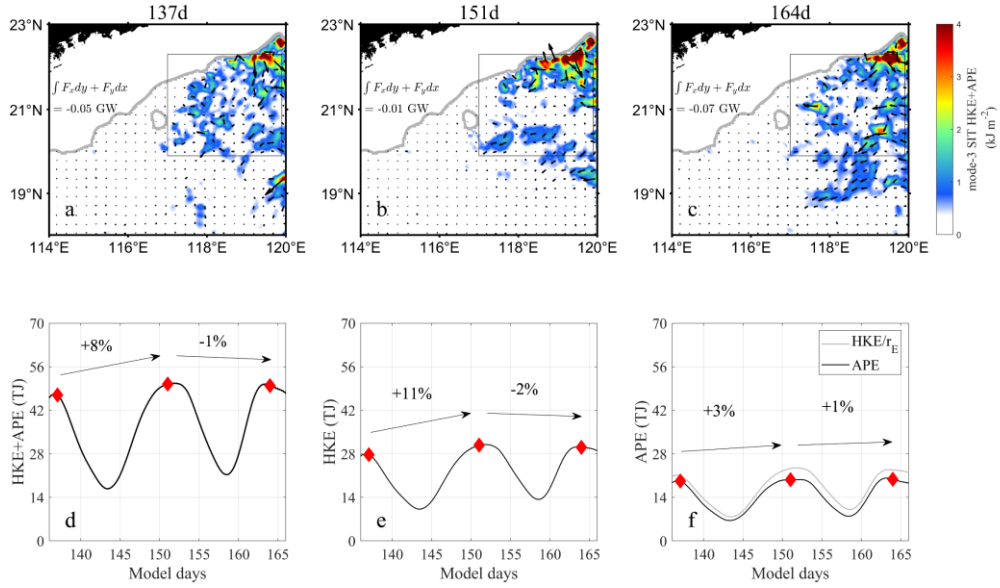
Figure 5. Same as Fig.3, but for mode-3 SIT.

Table 1. Sectional integrated energy flux (EF) and total energy (TE) of the first three modes of SITs on days 137 and 151. The percentage represents the relative change from day 137 to day 151.

	EF (GW)		relative	TE (TJ)		relative
	137d	151d	change	137d	151d	change
Mode1	3.15	4.31	37%	414	523	27%
Mode2	0.45	0.60	33%	158	189	20%
Mode3	0.05	0.01	-80%	47	50	8%

The impacts of the AE on SIT energy are outlined in Table 1. Day 137 serves as a reference when there was no effect from the AE, and day 151 is taken as the result under the influence of the AE. For the external input part (EF), mode 1 grew by 37% during the AE period, mode 2 increased by 33%, while mode 3 decreased by 80%. The external energy input of the SIT came mainly from the LS (the generating site); in comparison, the contribution of the AE was negligible. Regarding TE, mode 1 increased by 27%, mode 2 increased by 20%, and mode 3 had an increase of 8%. If the dissipation of the SIT (e.g., topographic drag friction and wave-wave interaction) is assumed to be a fixed proportion of the EF, the relative change for the TE of mode-1 SIT should be 37%; however, it was only 27%. This suggests that another type of interaction may have inhibited the overall growth of mode-1 TE. For example, transferring energy to higher-mode SIT ultimately led to a decrease in low-mode TE (Dunphy and Lamb, 2014; Dunphy et al., 2017; Huang et al., 2018). Convincing evidence is that mode-3 SIT realized an inverse increase in TE when the external energy input was reduced.

3.1.2 Contribution of topographic conversion

Second, we analyse the contribution of the topographic conversion term. The spatial distributions of the first three modes on day 151 are shown in Fig. 6a-c. The topographic conversion term for mode 1 is mostly negative, with most of the local minimums occurring at water depths of 250-2000 m. The situation is different for mode 2; it is primarily positive in the areas where mode 1 has local minimums, and it also contains regions with negative values. The distribution of mode 3 is similar to that of mode 2, except that its positive values cover a larger region than mode 2's, and its negative values have smaller amplitude and coverage than mode 2. Figures 6a-c indicate that during the AE period, topographic conversion manifested as low-mode SIT scattering toward higher modes.

Figures 6d-f show area integral over the region R2. Figure 6d shows the results of mode 1, with a trough during the AE period on day 151. Calculations indicate that a total of 0.93 GW energy was scattered into higher-mode SIT on day 151, while only 0.58 GW was scattered on day 137. Thus, the AE enhanced the topographic scattering of mode 1 by 60%. This might be one of the energy sinks of mode-1 SIT, resulting in a smaller relative increase in its TE than in its EF during the AE period, as shown in Fig. 3 and Table 1. Figure 6e shows the results for mode 2, where the integrated energy was comparable on day 151 (0.25 GW) and day 137 (0.21 GW), indicating that mode 2 gained energy from mode 1 while simultaneously scattering energy to higher modes, resulting in only a slight increase in its energy. Finally, Fig. 6f suggests that mode-3 energy increased significantly during the AE period (from 0.26 GW on day 137 to 0.44 GW on day 151), totalling an increase of 0.18 GW or a growth rate of 69%. This result is consistent with those in Fig. 5 and Table 1, which concludes that when the AE appeared within the region R2, there was a local energy source of mode 3, i.e., energy from low-mode topographic scattering.
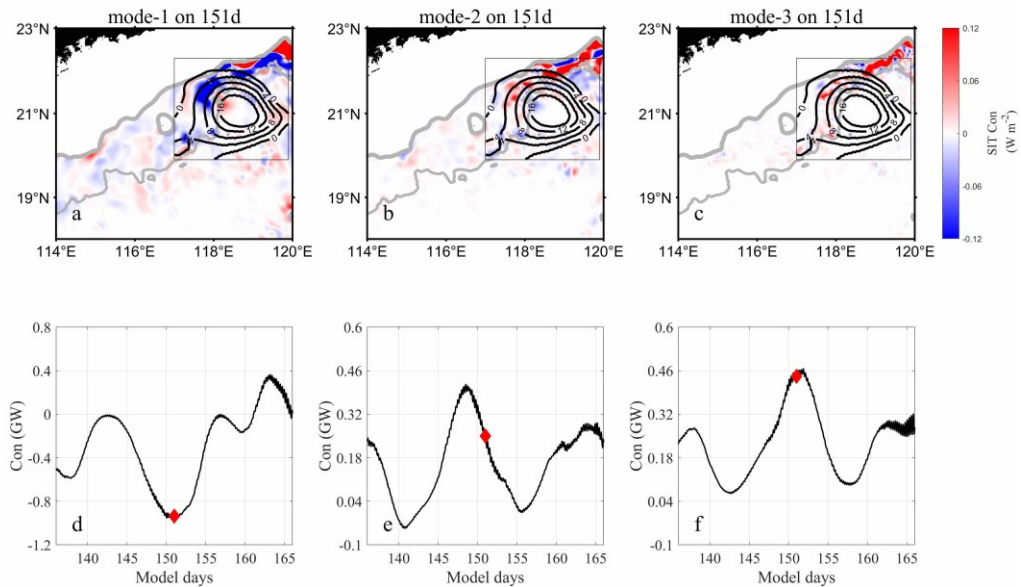
Figure 6. Spatial distribution of topographic conversion term for mode-1 to mode-3 SIT on day 151 in panels **(a-c)**. Panels **(d-f)** show the time series of their area integrals over the region R2. The red diamond indicates the result on day 151. The thick grey contour in **(a-c)**

indicates the depth of 250 m, and the thin grey contour indicates the depth of 2000 m. Note that **(d)** has a different y-axis labelling with **(e)** and **(f)**.

Figure 7 presents that C_{mn} is antisymmetric ($C_{mn} = -C_{nm}$, $C_{mm} = 0$). Generally, the values of C_{mn} for m=1:4 and $m<n$ are
235   positive (except for $C_{1,5}$ on day 164), which means that low modes transfer energy to higher modes. At the same time, the energy conversion between adjacent modes was usually more significant than those between nonadjacent modes. Besides, the energy conversion between adjacent modes (such as $C_{1,2}$, $C_{2,3}$, $C_{3,4}$, and $C_{4,5}$) were all the largest on day 151 compared to days 137 and 164. This indicates that the AE promoted downscale energy transfer between different SIT modes and efficiently scattered low-mode energy into higher modes (Hu et al., 2020; Löb et al., 2020), which is conducive to turbulence dissipation
240   process of SIT (Fernández-Castro et al., 2020). Figure 6e shows that the topographic conversion of mode 2 reached its maximum value on day 148 rather than on day 151. This is a result of the competition between two processes: acquiring energy from lower modes ($C_{0,2}$ and $C_{1,2}$) and scattering energy to higher modes ($C_{2,3}$, $C_{2,4}$, $C_{2,5}$). We calculate $\sum_{m=0}^{5}\langle C_{m,2}\rangle$ on day 148 based on Fig. 7c and obtain a value of 11.31 mW m^{-2}, which is larger than that on day 151 ($\sum_{m=0}^{5}\langle C_{m,2}\rangle$ = 6.33 mW m^{-2} based on Fig. 7b).
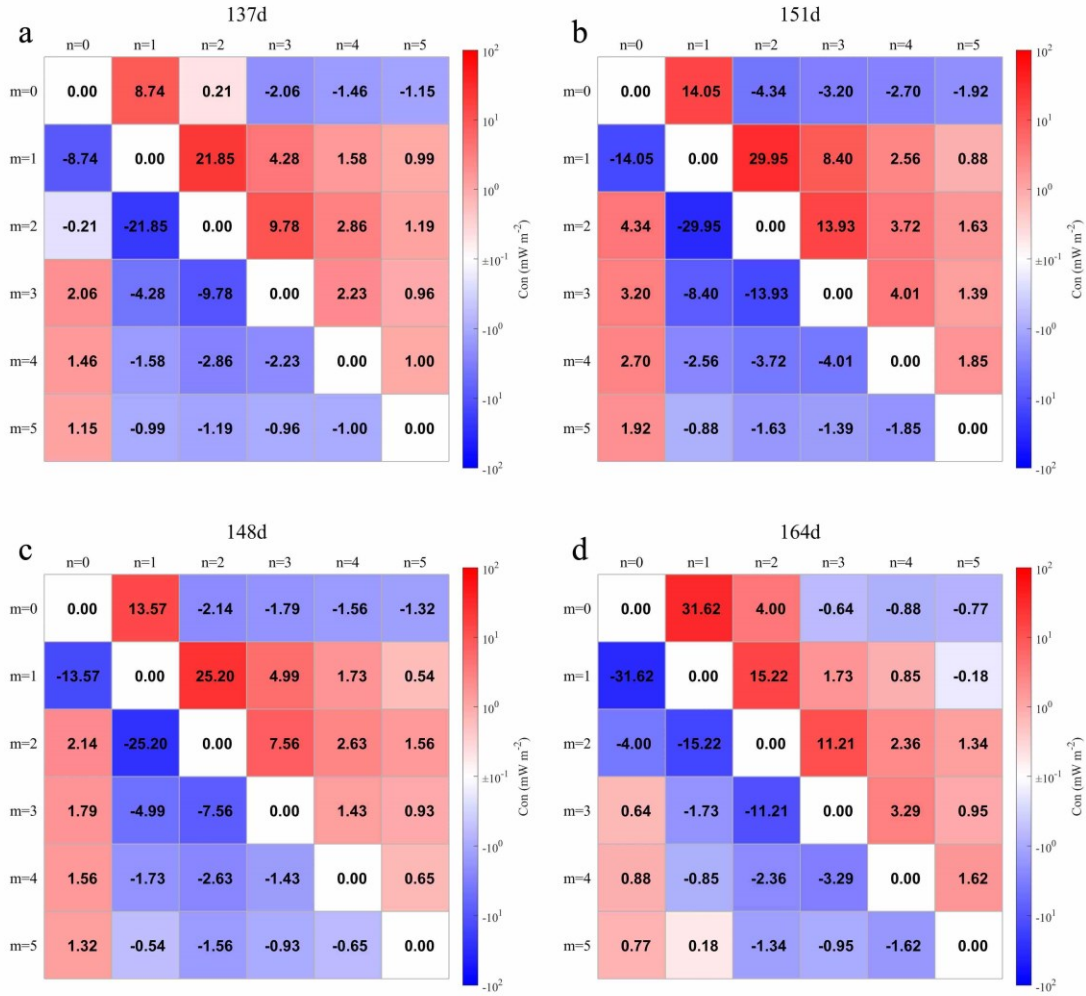
Figure 7. Distributions of topographic conversion term C_{mn} (spatially averaged over the region R2 with water depths between 250 and 2000 m; in log scale) in the domain of mode number on days 137, 151, 148, and 164. Subscripts m and n represent the work done by mode m on mode n. Noted that, mode 0 represents the BT.

However, we have observed that values of $C_{0,3-5}$ were negative on day 151, in contrast to the results obtained on seamounts by Lahaye et al. (2020). Based on the direction of energy fluxes (Fig. 8c-e), it shows that the transmitted modes 3-5 SITs propagated northward, whereas the locally-generated modes 3-5 SITs propagated southward, leading to the negative values of $C_{0,3}$, $C_{0,4}$ and $C_{0,5}$ in this region (transmitted and locally-generated energy fluxes are in the opposite directions). Negative values of the conversion rate indicate that the internal tide energy is transferred to the barotropic tide through pressure work, which is not involved in turbulent kinetic energy dissipation (Zilberman et al., 2009). In addition, negative conversion rates have been found in some studies, e.g., Figure 5 of Song and Chen (2020), Figure 6 of Wang et al. (2016), and Figure 9 of Xu et al. (2016).

In order to explore the reason for the enhanced topographic scattering from low-mode to higher modes in the presence of the AE, we calculate the cross-shore energy flux for the first five modes of SITs (Fig. 8 and Fig. 9). For mode 1, the cross-shore flux was 3.19 GW and the along-shore value was 1.06 GW on day 137, resulting in a reflection of 33%; on day 151, the cross-shore energy flux was 5.22 GW and the along-shore value was 1.52 GW, with a reflection of 29%, decreasing by 4%. For mode 2, the cross-shore energy flux was 0.31 GW and along-shore value was 0.10 GW on day 137, with a reflection of 32%; on day 151, the cross-shore energy flux was 0.70 GW and along-shore value was 0.31 GW, with a reflection of 44%. The cross-shore energy flux for modes 3-5 on day 137 were 0.03 GW, 0.01 GW, and 0.01 GW, respectively, while the cross-shore values on day 151 changed to 0.08 GW, 0.02 GW, and 0.01 GW. As a result, we inferred that the increased higher-mode SIT energy flux on the continental slope came from the mode-1 SIT (5.22×4%=0.209 GW, 0.70×12%+0.05+0.01=0.144 GW), which may be due to transmission of the mode-1 SIT as it passed the subcritical continental slope, transferring energy to higher modes. It can be checked by Fig. 8 that modes 3-5 have remarkable energy flux vectors between the critical topography ($\gamma=1$; magenta curve) and the 2000 m isobath. It is also reported that the low-modal internal tides passing through the subcritical continental slope topography are more susceptible to transmission (Hall et al, 2013; Wang et al., 2018 and 2019), consistent with our results.
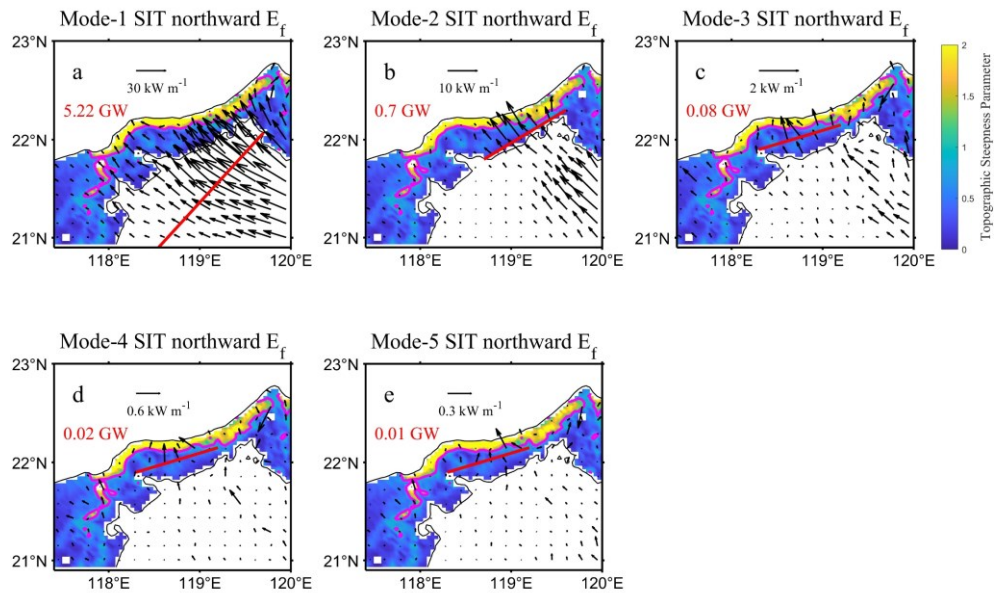
Figure 8. Spatial distribution of the northward component (incident wave) of the energy flux (arrows) for the first five modes of SITs on day 151, superimposed on the contour map of topographic steepness parameters from 250 to 2000 m, with magenta contour for $\gamma = 1$. The red values in the upper left are calculated by integrating energy flux along the section (red line).
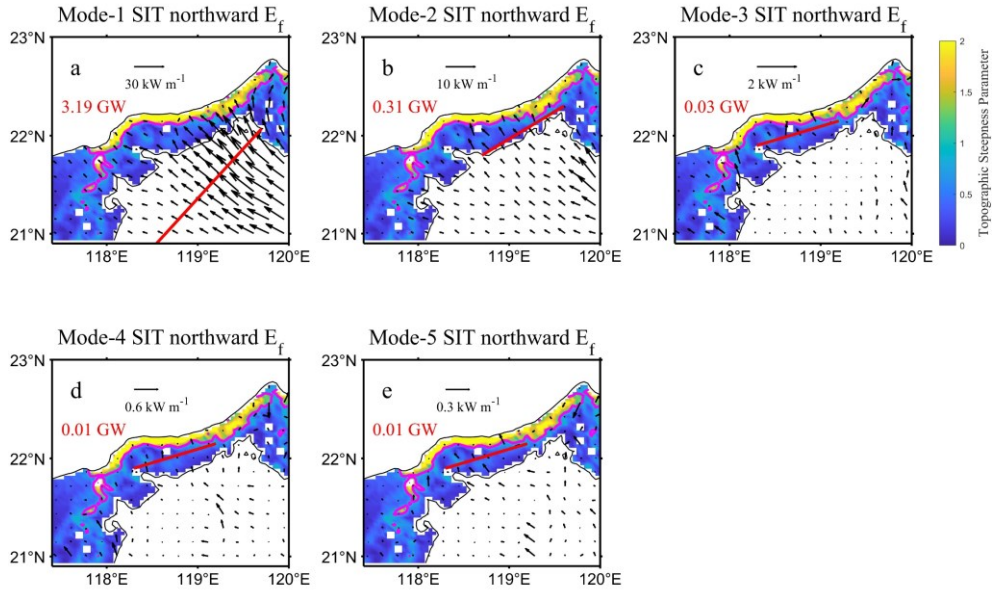
275

Figure 9. Same as Fig. 8, but for day 137.

3.1.3 Contribution of advection by the AE

Next, we analyse the impact of the advection term on SIT's energy changes. Using Eq. (A2), we find that the advection term consists of two parts, one part related to the baroclinic velocity of SIT, called A_{mn}^u, and the other related to the pressure perturbation of SIT, called A_{mn}^p. The results of A_{mn}^u are shown in Fig. 10. As the mode number increases, the amplitude of A_{mn}^u decreases, because the low-mode ITs have larger velocities and more energy (Liu et al., 2019). Figures 10a-b present that the advection was most intense around the AE, with roughly alternating positive and negative distributions along the sea-level anomalies (SLA) contours, which is consistent with the findings of Dunphy and Lamb (2014). The R2 area integrals (Fig. 10d-f) show that positive and negative values vary symmetrically along the zero line, with peak or trough appearing during the AE period. Adding up the positive and negative values, we find that the advection term weakened the energy of mode 1 (note that the advection term appears on the left side of Eq. (1), so a positive value represents a decrease in IT energy), and enhanced the energy of modes 2 and 3. The results for A_{mn}^p (Fig. 11a-c) have similar spatial distribution patterns to those of A_{mn}^u, but with smaller amplitude, implying that the velocity component of the advection was dominant. This conclusion is also applicable when integrating over space (Fig. 11d-f). The effects of A_{mn}^p on the first three modes of SITs are similar to those of A_{mn}^u.
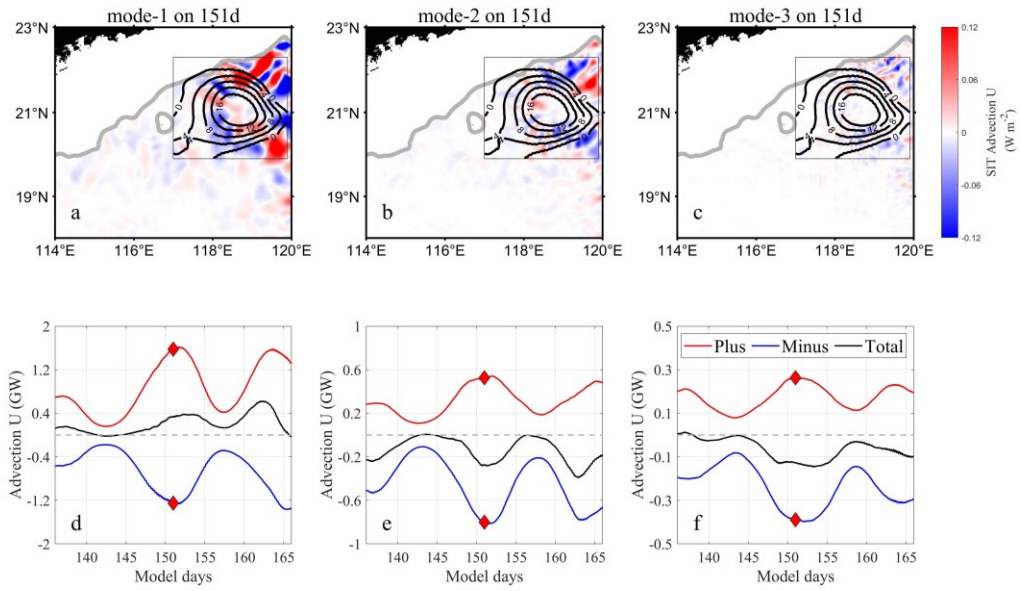
Figure 10. Same as Fig. 6, but for the velocity component of the advection term of SIT. The red, blue, and black curves in **(d-f)** represent the R2 area integral results of positive, negative, and all values within the rectangle, respectively.
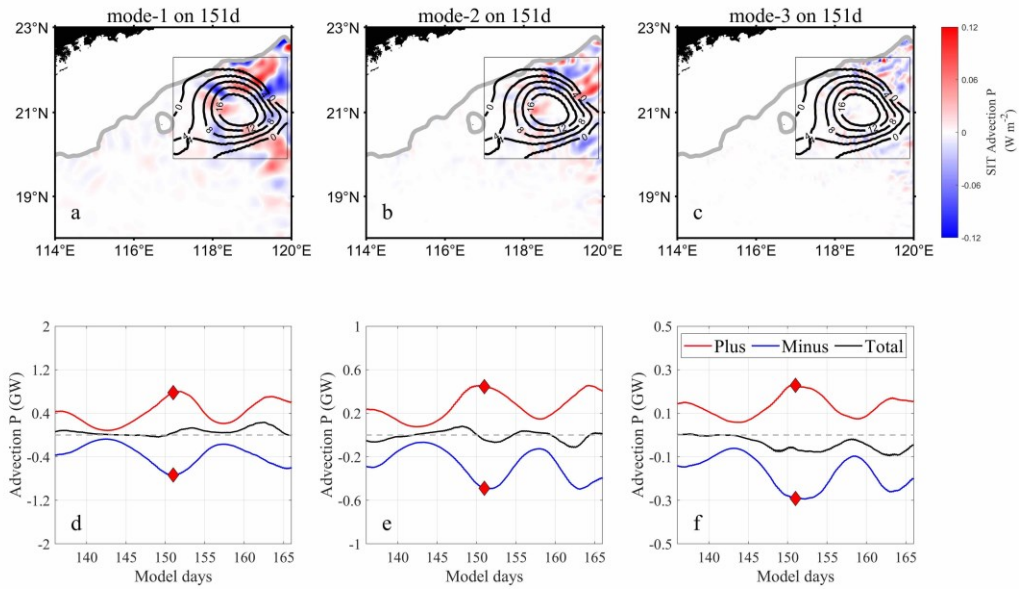
Figure 11. Same as Fig. 10, but for the pressure component of the advection term of SIT.

290

3.1.4 Contribution of energy exchange between AE and SIT

Finally, we analyse the impact of the energy exchange term on SIT's energy changes. The energy exchange term can be subdivided into horizontal shear production, vertical shear production, and horizontal buoyancy production (Fig. 12). The greater the mode number, from left to right in Fig. 12, the weaker the energy exchange. The magnitude of the vertical shear production is the largest of the three components, implying that the vertical shear of the eddy field dominates the energy exchange between the AE and SIT. In terms of the R2 area integrals (Fig. 13), the temporal trend of mode 1 is similar to that of the advection term (Fig. 10 and Fig. 11), with extremes during spring tides; mode 2 exhibits peak or trough only on day 151, and mode 3 has no prominent peak. During the AE period, shear production led to negative/upscale energy exchange (from the IT field to the eddy field); conversely, buoyancy production mainly induced positive/downscale energy exchange (from the eddy field to the IT field). Overall, there was a net energy exchange from the IT field to the eddy field during the AE period, with a regional average rate of 3.0 mW m^{-2} on day 151 (the sum of the energy exchange terms of the first three modes divided by the square of R2, $\sum_{n=1}^{3}(P_n^s + P_n^b)/S$). This is quite close to the result of -2.2±0.6 mW m^{-2} obtained by Cusack et al. (2020) in the Southern Ocean, which suggests that the IT field may act as an energy source for the eddy field.

We tracked the eddy energy tendency and found that, in the first 20 days, the tendency increases with time, consistent with the change of shear production, but in the last 20 days, the tendency decreases with time, opposite to the change of shear production (not shown). We think this may be due to other dynamic motions in the northern SCS such as Kuroshio intrusion, submesoscale motions and internal waves at various frequency bands, which contribute to variations in EKE along with SIT-to-eddy conversion discussed here accounting for a fraction of total energetics (i.e., Liu et al., 2022).
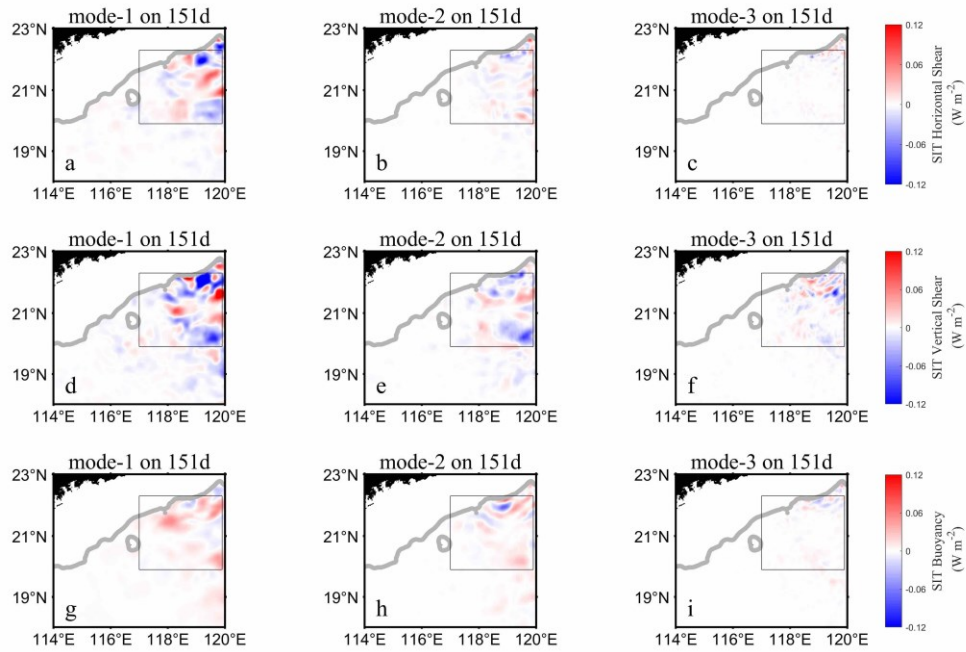
Figure 12. Spatial distributions of the first three modes of SITs on day 151, with **(a-c)** representing horizontal shear production, **(d-f)** representing vertical shear production, and **(g-i)** representing horizontal buoyancy production.
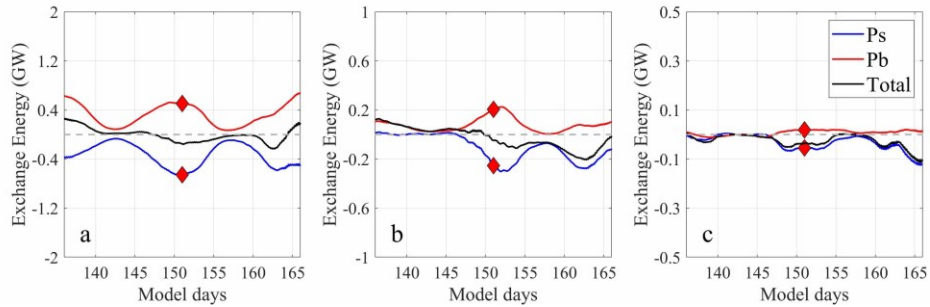
Figure 13. Time series of spatial integration for the first three modes **(a-c)**, with Ps representing the sum of the horizontal and vertical shear production terms, Pb representing the horizontal buoyancy production, and Total being their sum.

3.2 Effects of the AE on kinematic properties of SIT

3.2.1 Impact of the AE on low-mode SIT reflection over continental slope

During the propagation of low-mode SITs, different types of continental slope topography may be encountered. According to the topographic steepness parameter,

$$\gamma = \frac{|\nabla H|}{\sqrt{\frac{\omega^2 - f^2}{N^2 - \omega^2}}}, \tag{3}$$

where H is water depth, topography can be classified into three types: subcritical topography ($\gamma<1$), where IT can continue to propagate and shoal onto the continental slope; critical topography ($\gamma=1$), where IT is captured by the topography and subsequently breaks; and supercritical topography ($\gamma>1$), where internal tidal rays are reflected by the continental slope (Pedlosky, 2003; Kelly et al., 2013; Legg, 2014).

We focus on the energy reflection of mode-2 SIT on a supercritical continental slope, as Fig. 4b shows that part of its energy is reflected on the slope. First, we adopt a directional Fourier filter method (DFF; Gong et al., 2021) to decompose the baroclinic velocity ($\boldsymbol{u}$) and pressure perturbation (p) of SIT into incident and reflected components:

$$\begin{cases} \boldsymbol{u} = \boldsymbol{u}_i + \boldsymbol{u}_r \\ p = p_i + p_r \end{cases}, \tag{4}$$

where subscripts i and r represent incident and reflected components, respectively. Then, the energy fluxes of incident and reflected waves are calculated as follows:

$$\begin{cases} \boldsymbol{F}_i = \boldsymbol{u}_i p_i \\ \boldsymbol{F}_r = \boldsymbol{u}_r p_r \end{cases}, \tag{5}$$

Wang et al. (2020) concluded that the DFF method is suitable and most effective for processing 3D numerical model outputs after comparing three different decomposition methods.

The first three modes of SITs all had topographic reflection when encountering supercritical continental slope topography (see Fig. C1 and Fig. C2 in Appendix C), but here we focus our analysis on the mode 2, which shows an enhancement in reflection in the presence of the AE.

Figure 14a depicts the total energy flux of mode-2 SIT on day 151 (under the influence of the AE), demonstrating that the energy flux propagating northwestward may be reflected on the continental slope (near 119° E, 22° N). It is worth noting that the result for the energy flux of mode-2 SIT is slightly different from the earlier studies (Kerry et al., 2013; Xu et al., 2021), because their work considered the energy flux of all modes. To verify this reflection phenomenon, we examine the energy fluxes along the incident and reflected directions in Fig. 14b-c, respectively. According to the incident energy flux integrated along section S1, a total of 0.70 GW mode-2 SIT propagated toward the continental slope (Fig. 14b). The reflected energy flux integrated along section S2 implies that there was a total of 0.31 GW mode-2 SIT energy being reflected off the continental slope with a reflection coefficient of 44% (Fig. 14c). However, there were 0.31 GW along section S1 and 0.10 GW along section S2, with a reflection coefficient of just 32% on day 137 (without the AE). We compare the reflection coefficient, which was 32% on day 137 and increased to 44% on day 151, increasing by 12% under the influence of the AE (on day 151), implying that the AE promotes a reflection of mode-2 SIT. Previous studies showed that the magnitude of the reflection coefficient is closely related to the steepness of the continental slope; for example, on the supercritical Tasmanian continental slope, the reflection coefficient of SIT can exceed 60%, forming a distinct standing wave structure (Johnson et al., 2015; Klymak et al.,

2016; Zhao et al., 2018). The spatial distribution of topographic steepness parameters during the AE period (Fig. 14d) also indicates that the continental slope was mainly supercritical for SIT, which favored the reflection of SITs.
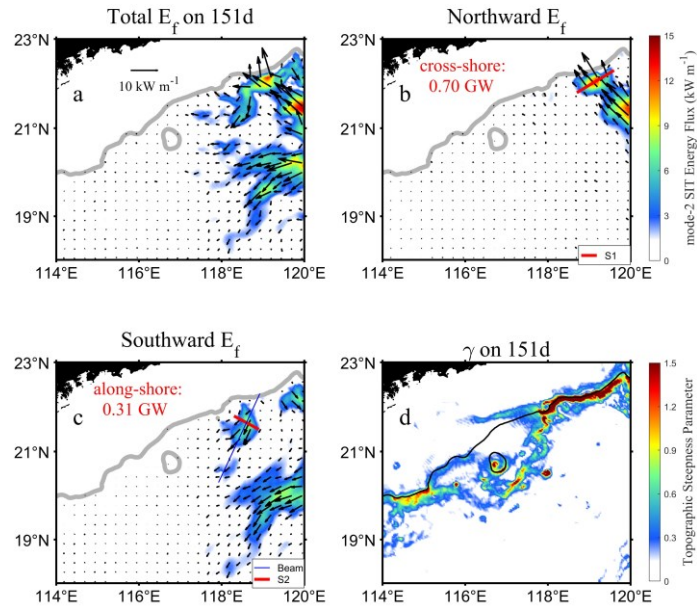
Figure 14. The energy flux of mode-2 SIT on day 151 in **(a)**, **(b)**, and **(c)** for total, northward, and southward, respectively. The energy fluxes integrated along sections S1 and S2 are labelled as cross-shore and along-shore values, respectively. The topographic steepness parameter for SIT on day 151 is presented in **(d)**.

Through theoretical wave ray calculations (Eq. (6)), we find that mode-2 SIT was reflected from the shallow supercritical

360   continental slope to the deep-sea basin of the SCS. Although the paths of the wave rays were similar, the propagation distance of wave rays on day 151 was somewhat longer than that on day 137 (Fig. 15). Besides, the mode-2 baroclinic velocities visually demonstrate that the energy of the reflected mode-2 SIT was significantly enhanced under the impact of the AE (maximum amplitude of 0.16 m s^{-1} on day 151 and 0.09 m s^{-1} on day 137), indicating that the AE promoted mode-2 SIT reflection.

$$\frac{dz}{dx} = \sqrt{\frac{\omega^2 - f^2}{N^2 - \omega^2}} \qquad\qquad\qquad (6)$$

365
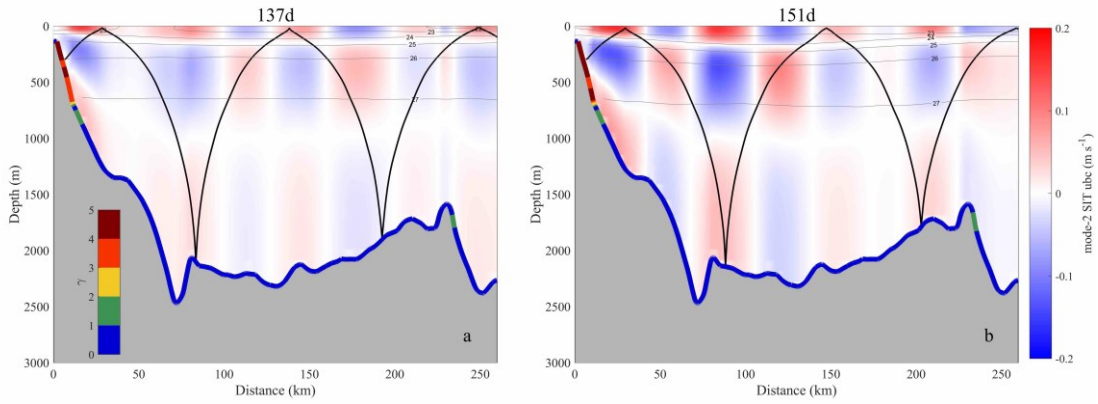
Figure 15. The baroclinic velocity of mode-2 SIT on days **(a)** 137 and **(b)** 151 along the Beam section shown in Fig. 14c. Black curves are theoretical wave rays (assuming that mode-2 SIT propagates mainly from the continental slope where the topographic steepness parameter is greater than 1, and then integrating the Eq. (6) over time), and grey contours are isopycnals (ρ-1000). The colors marked along the seafloor represent the values of the topographic steepness parameter.

370   Regarding the reason for enhanced reflection of mode 2, we use the rose diagram and topographic steepness parameter (Fig.

16) to explore it.
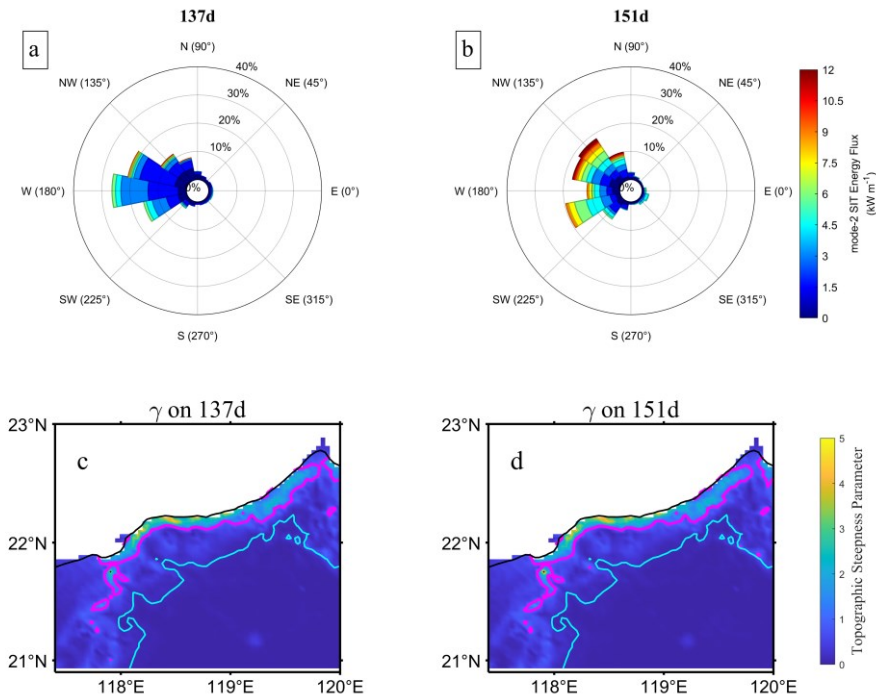
Figure 16. (a-b) The rose diagrams for the mode-2 SIT on days 137 and 151, respectively, the selected region is (119-120° E, 19.9-22.3° N). **(c-d)** The topographic steepness parameter for days 137 and 151, respectively, magenta line for γ=1 and cyan line for the 2000 m isobath.

375   Figures 16a-b demonstrate that the AE has a significant impact on the propagation direction of the mode-2 SIT. On day 137, the mode-2 SIT mainly propagated toward west (180°) and west-northwest (157.5°). It is generally parallel to the critical topography (magenta curve) with a nearly east-west orientation around 119°E. Therefore, the topographic reflection was suppressed due to the angle of the incident waves on day 137. In contrast, on day 151, the mode-2 SIT was deflected by AE towards the continental slope, and its propagation direction changed to northwest (135°) and west-northwest (157.5°). The

380   angle between mode-2 SIT's propagation direction and critical topography (magenta curve) increases, which facilitates the reflection of mode-2 SIT. By comparing the topographic steepness parameter on days 137 and 151 (Fig. 16c-d), we find that their differences are slight (the magenta curves in these two panels are almost identical), because stratification doesn't change significantly in half a month, suggesting that enhanced reflection of mode 2 is due to the change of incident angle caused by refraction of the mode-2 SIT due to eddy.

385   **3.2.2 Effect of the AE on low-mode SIT propagation and refraction**

Here, we study the impact of the AE on SIT propagation and refraction. As is well known, the greater the mode number of IT, the shorter the propagation distance. For high-mode ITs (mode number ≥4), their propagation distances cannot exceed $1/2°$ (about 50 km), so they contribute to near-field dissipation at their generation sites (St. Laurent and Garrett, 2002; Vic et al., 2019). Unlike high-mode ITs, low-mode ITs dissipate in far-field regions and are therefore more susceptible to interference

390   from background oceanic motions during their propagation. As a result, it is challenging to predict the propagation of low-mode SITs accompanied by the occurrence of tidal nonstationarity and incoherent processes (Whalen et al., 2018; Savage et al., 2020). The spatial distribution of tidal-induced mixing in the ocean is affected by the propagation path and distance of SIT, which is critical to the formation of deep-sea overturning circulations (You et al., 2022, 2023; Zhou et al., 2023).

The phase speed is a useful variable for studying the propagation of SIT. When considering the influence of background

395   flow, we usually obtain the eigenvalues by solving the Taylor-Goldstein equation (Smyth et al., 2011). However, the equation does not take into account the Coriolis effect; hence, a correction for Earth rotation effects is introduced (Zhao et al., 2010), which yields Eq. (7),

$$\begin{cases} \frac{d^2\Phi_n}{dz^2} + \left[\frac{N^2}{(U-c_n^U)^2} - \frac{d^2U/dz^2}{U-c_n^U} \right] \Phi_n = 0 \\ c_p^U = \frac{\omega}{\sqrt{\omega^2-f^2}} c_n^U \end{cases} , \qquad (7)$$

where Φ_n indicates the eigenfunction of vertical structure, subscript n represents the nth mode, and N^2 indicates the buoyancy

400   frequency squared. c_n^U and c_p^U are the eigen speed and phase speed, respectively, considering both the stratification and background flow. If we exclude the impact of the background flow, Eq. (7) can be simplified to Eq. (8),

$$\begin{cases} \frac{d^2\Phi_n}{dz^2} + \frac{N^2}{c_n^2} \Phi_n = 0 \\ c_p = \frac{\omega}{\sqrt{\omega^2-f^2}} c_n \end{cases} , \qquad (8)$$

where c_n and c_p are the eigen speed and phase speed, respectively, considering only the stratification.

To more intuitively describe how SITs propagate under different background conditions, we use Park and Farmer's (2013)
method to calculate the ray paths for SITs. At the same time, to consider the interactions among mode 1, mode 2, and the AE, we select two ray starting points. The north starting point is located at (119.8° E, 21.5° N), with an initial angle of 170° (east corresponds to 0°, counterclockwise rotation). The south starting point is at (119.8° E, 20.5° N), and the initial angle is 185°.

We studied the influence of the AE on the propagations of mode-1 and mode-2 SIT. Figure 17 shows the SIT phase speed calculated by using Eq. (8), considering only the AE-associated stratification. During the period of the AE (on day 151; Fig. 17b and Fig. 17e), the propagation distance of first two modes of SITs is close to that of day 137 (Fig. 17a and Fig. 17d); meanwhile, the north ray was shifted by 5° and the south ray was shifted by 8° for mode 1, while the two rays of mode 2 showed little variation. These results suggest that AE's short influence distance (limited by AE diameter) did not significantly affect the propagation of the first two modes of SIT.
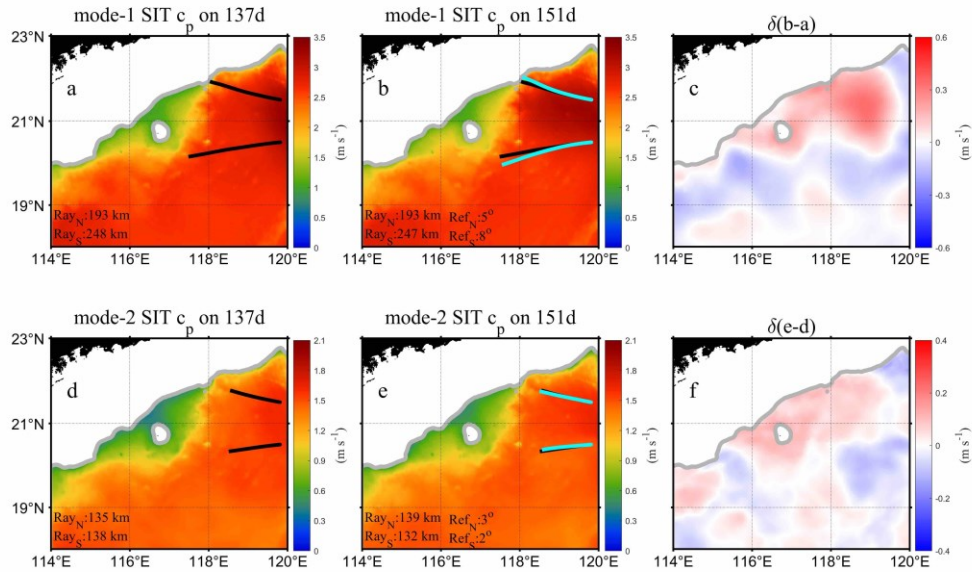
Figure 17. Spatial distributions of phase speeds (only considering the stratification) of mode-1 and mode-2 SITs on days 137 and 151. **(c)** and **(f)** represent the differences between days 151 and 137. The black and cyan curves are the propagation rays of SITs during days 137 and 151, respectively.

Figure 18 compares the SIT phase speeds without and with the impact of AE velocity, demonstrating that the northern part of the AE's velocity field can lower the SIT phase speed in the region of (118°-119.9° E, 21.2°-22.3° N), with the mean decreases of modes 1 and 2 being -0.20 and -0.12 m s^{-1}, respectively. The SIT phase speed increased in AE's southern part, especially in the region of (118°-119.9° E, 19.9°-21.2° N), with the mean increases of modes 1 and 2 being 0.47 and 0.30 m s^{-1}, respectively. The SIT rays on day 151 calculated using c_p and c_p^U are shown as black and cyan curves in Fig. 18b and Fig. 18e, from which two significant features can be identified. One is that the propagation distance of the north ray was shortened,

while that of the south ray was lengthened. The other effect is that the AE velocity field magnified both the northward deflection of the north ray and the southward deflection of the southern ray. Zhao (2014) found that the propagation of diurnal ITs (e.g., K_1 and O_1) in the SCS is deflected toward the equator (its phase speed decreases with latitude). Under the influence of the AE, the latitudinal distribution of phase speed was altered (a local maximum occurred on the southern side of the AE and tended to decrease toward both north and south directions), which resulted in the SIT refracted toward both north and south directions, because SIT propagation follows the direction of group velocity (along which phase speed decreases).
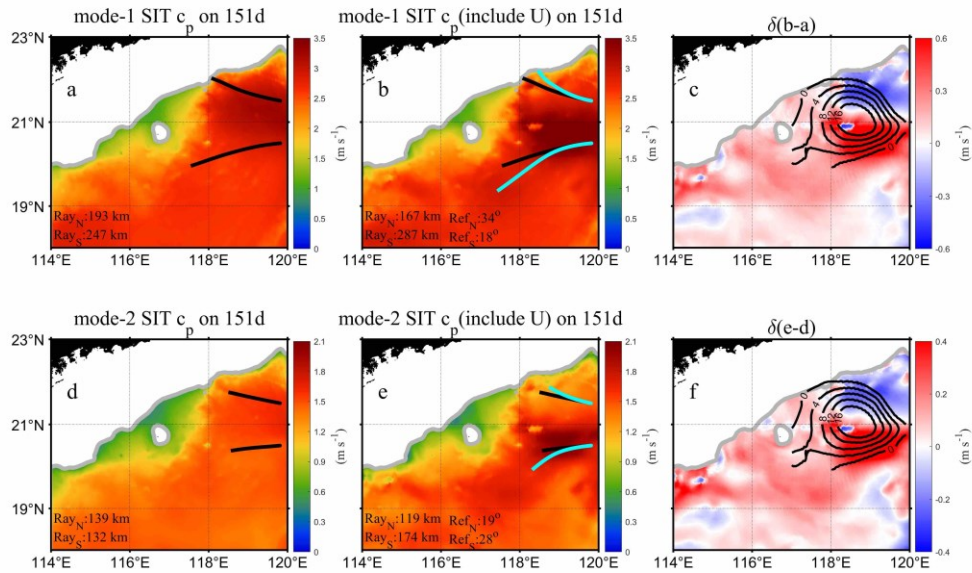
Figure 18. Spatial distributions of mode-1 and mode-2 SIT phase speeds on day 151. **(a)** and **(d)** are the same as Fig. 17b and Fig. 17e for c_p without the effect of the background flow; **(b)** and **(e)** are c_p^U considering the effect of the background flow; **(c)** and **(f)** indicate the difference between the first two modes c_p^U and c_p; and black contours represent SLA on day 151.

Zaron and Egbert (2014) proposed that the relative perturbations of phase speed ($\delta c_p / c_p$) are mainly composed of three portions, namely, perturbations in stratification, and advection and shear of the background flow. Their results indicated that stratification and advection are the dominant factors for the change of phase speed along the Hawaiian Ridge. The same finding was obtained by Savage et al. (2020) in the Tasman Sea in the southwestern Pacific Ocean. The results of our analysis shown above are consistent with these published ones.

4 Discussion

Kelly et al. (2012) introduced the topographic conversion term to quantify the work done by the mode-m IT on mode-n IT, which is related to topography and background stratification (Kelly et al., 2013). The background temperature-salinity field is altered by ME (Hu et al., 2011; Chu et al., 2014; Fernández-Castro et al., 2020). Therefore, the topographic conversion term

is one of the contributions of interaction. In addition, the advection and energy exchange terms are directly related to the velocity field of ME. Unlike the energy exchange term, the advection term does not involve energy transfer between ME and

445 IT. In other words, the advection term's energy comes from IT, whereas ME just induces refraction of IT energy (Zaron and Egbert, 2014; Kelly et al., 2016b; Wang et al., 2021). Next, we discuss their relative importance.
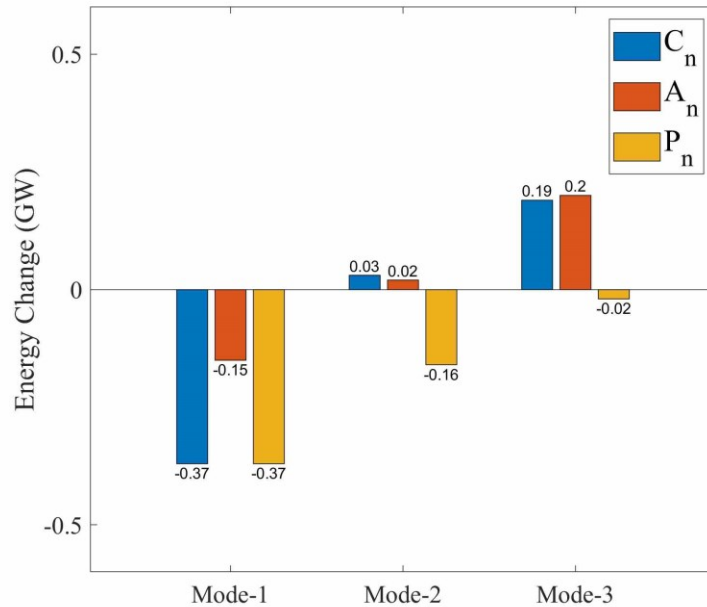
Figure 19. Changes in topographic conversion term (C_n), advection term (A_n), and energy exchange term (P_n) for the first three modes on day 151 compared to those on day 137.

450   The above results (Fig. 6, Fig. 10, Fig. 11, and Fig. 13) present that among the three main contribution terms, the amplitude of the advection terms ($A_{mn}^u + A_{mn}^p$) is the largest on day 151, followed by that of the topographic conversion term and energy exchange term. However, different conclusions can be drawn in terms of their absolute changes on day 151 relative to day 137 (Fig. 19). Although the advection term had the largest amplitude, its absolute change was minor, while a larger change existed in the topographic conversion and energy exchange terms during this period. Figure 19 illuminates that the advection and

455 topographic conversion terms had similar changing trends (decreasing in mode 1, increasing in modes 2 and 3), but the absolute change in the topographic conversion term was significantly larger. Nevertheless, the absolute change in energy exchange term decreased with the increase of mode number, but it was negative for modes 1-3, indicating energy transfer from IT to ME. These results suggest that when the AE and SIT interacted near the continental slope, the variation of energy in the first three modes of SITs was mainly dominated by topographic conversion and energy exchange, rather than by advection.

5 Conclusions

Using a high-resolution dataset of 3D numerical model, we investigated the interaction processes between an AE and SIT on the continental slope of the northeastern SCS. The main conclusions are as follows.

The interaction between the AE and SIT changed the magnitude of SIT energy. Using the energy equation of IT with ME, we quantified the contributions of three interaction terms. It is evident that the effects of the topographic conversion and energy exchange (including shear production and horizontal buoyancy production) terms on SIT energy far outweighed that of the advection term. Additionally, the AE promoted topographic inter-modal scattering and facilitated downscale cascade of SIT energy on the continental slope, which drove energy conversion from mode-1 SIT to higher-mode SITs. Moreover, energy was transferred from the IT field to the eddy field at an average rate of 3.0 mW m^{-2}, mostly via vertical shear production. The advection term weakened mode-1 SIT energy while enhancing mode-2 and mode-3 SIT energy, with velocity-associated advection dominating pressure-related advection.

The interaction not only changed the SIT energy but also modulated the propagation of low-mode SITs. The analysis based on the Taylor-Goldstein equation confirms that the currents related to the AE have a more significant impact on altering SIT's phase speed than eddy-associated stratification variation. The eddy currents decreased SIT's phase speed on AE's north side, while increasing it on AE's south side. Consequently, the SIT propagation distance is found to be shorter on AE's north side than on the south side at the same time. In addition to causing refraction of low-mode SITs, the interaction may also enhance the reflection of low-mode SITs near the supercritical continental slope. The AE was found to intensify the energy of the reflected mode-2 SIT, increasing the reflection coefficient from 32% (pre-AE) to 44% (during the AE period), which is due to the change of incident angle caused by refraction of the mode-2 SIT due to eddy.

In summary, the interaction between the AE and SITs altered the energy and propagation of SITs in the SCS, thereby affecting the spatial distribution of tidal-induced turbulent dissipation. Therefore, comprehending the physical mechanism behind their interaction is instructive for parameterization and forecasting of ITs.

Limited by the length of the article, we only analyzed the interaction between the AE and SITs. We plan to investigate the interaction between eddy of other polar (e.g., cyclonic eddy) and (semidiurnal or diurnal) ITs in the future.

Appendix A

The normalized eigenfunction from Eq. (8) satisfies the orthogonal condition:

$$\begin{cases} \int_{-H}^{0} \Phi_m \Phi_n N^2 dz = c_n^2 H \delta_{mn} \\ \int_{-H}^{0} \phi_m \phi_n dz = H \delta_{mn} \end{cases}, \tag{A1}$$

where δ_{mn} is the Kronecker delta (when $m \neq n$, δ_{mn}=0, when $m = n$, δ_{mn}=1).

The formulas for each term in Eq. (1) are as follows:

$$\begin{cases} \boldsymbol{F}_n = H\boldsymbol{u}_n p_n = \boldsymbol{U}_n p_n \\ A_{mn} = A_{mn}^u + A_{mn}^p = [(\overline{\boldsymbol{U}}_{mn} \cdot \nabla)\boldsymbol{U}_m] \cdot \frac{\boldsymbol{U}_n}{H} + (\frac{H}{c_n^2}\overline{\boldsymbol{U}}_{p,mn} \cdot \nabla p_m)p_n \\ C_{mn} = [T_{mn}(\boldsymbol{u}_m p_n) - T_{nm}(\boldsymbol{u}_n p_m)] \cdot \nabla H \\ P_{mn}^S = P_{mn}^{Sh} + P_{mn}^{Sv} = -(\boldsymbol{U}_m \cdot \nabla)\overline{\boldsymbol{U}}_{mn} \cdot \frac{\boldsymbol{U}_n}{H} + (\nabla \cdot \boldsymbol{U}_m)\overline{\boldsymbol{U}}_{z,mn} \cdot \frac{\boldsymbol{U}_n}{H} \\ P_{mn}^B = \left(\frac{\boldsymbol{U}_m}{c_n^2} \cdot \overline{\boldsymbol{B}}_{mn}\right) p_n \end{cases}, \tag{A2}$$

Where $\boldsymbol{u}_n$ and p_n are the mode-n amplitude of baroclinic velocity $\boldsymbol{u}$ and pressure perturbation p, respectively. C_{mn} is calculated by using Eq. (12) of Zaron et al. (2022). The operators $\overline{\boldsymbol{U}}_{mn}$, $\overline{\boldsymbol{U}}_{p,mn}$, $\overline{\boldsymbol{U}}_{z,mn}$, T_{nm}, and $\overline{\boldsymbol{B}}_{mn}$ are calculated as follows:

$$\begin{cases} \overline{\boldsymbol{U}}_{mn} = \frac{1}{H}\int_{-H}^{0} \overline{\boldsymbol{U}} \phi_m \phi_n dz \\ \overline{\boldsymbol{U}}_{p,mn} = \frac{1}{H}\int_{-H}^{0} \overline{\boldsymbol{U}} \frac{N^2}{c_m^2} \Phi_m \Phi_n dz \\ \overline{\boldsymbol{U}}_{z,mn} = \frac{1}{H}\int_{-H}^{0} \overline{\boldsymbol{U}} (\Phi_m \Phi_n \frac{N^2}{c_n^2} - \phi_m \phi_n) dz \\ T_{nm} = \begin{cases} \frac{1}{2}(1 - \phi_n^2)|_{z=-H}, n = m \\ \frac{c_n^2}{c_m^2 - c_n^2}\phi_n \phi_m|_{z=-H}, n \neq m \end{cases} \\ \overline{\boldsymbol{B}}_{mn} = \begin{cases} \frac{f}{H}\int_{-H}^{0} \overline{V}\left(\frac{N^2}{c_m^2}\Phi_m \Phi_n - \phi_m \phi_n\right) dz, \overline{B}_{x,mn} \\ -\frac{f}{H}\int_{-H}^{0} \overline{U}\left(\frac{N^2}{c_m^2}\Phi_m \Phi_n - \phi_m \phi_n\right) dz, \overline{B}_{y,mn} \end{cases} \end{cases}, \tag{A3}$$

where $\overline{\boldsymbol{U}}$ is the horizontal velocity of ME, $\overline{\boldsymbol{B}}_{mn}$ is related to ME velocity using thermal wind balance to reduce numerical errors caused by differential calculations (e.g., horizontal and vertical gradient operators) (Book et al., 1975; Lahaye et al., 2020). And c_n and c_m stand for eigen speed of the nth and mth mode, respectively.

The method (Kelly et al., 2012) calculating HKE and APE is:

$$\begin{cases} \mathrm{HKE}_n = \frac{\rho_0 H}{2}(u_n^2 + v_n^2) \\ \mathrm{APE}_n = \frac{\rho_0 H}{2}\left[\left(1 - \frac{f^2}{\omega^2}\right)\frac{p_n^2}{c_n^2}\right] \end{cases}, \tag{A4}$$

where ρ_0 is the reference density, ω is the frequency of IW.

 Appendix B

To evaluate the reasonableness of term $\langle D_n \rangle$ in Eq. (1), we estimated the energy dissipation of the model using the viscosity coefficient of MITgcm LLC4320. According to the official documentation (https://github.com/MITgcm-contrib/llc_hires/tree/master/llc_4320), the horizontal eddy viscosity coefficient is determined by the parameterization scheme, and the vertical eddy viscosity coefficient is $A_v=5.66\times10^{-4}$ m^2 s^{-1}. The horizontal diffusion coefficient is $K_h=0$ m^2 s^{-1}, and the vertical diffusion coefficient is $K_v=5.44\times10^{-7}$ m^2 s^{-1}. Because all diffusion coefficients for temperature and salinity are very small, they can be ignored in ε_{diff} term.

$$D = \varepsilon_{visc} + \varepsilon_{diff} + \varepsilon_{drag} \ , \tag{B1}$$

$$\varepsilon_{visc} = \rho_c A_h \left[\left(\frac{\partial u}{\partial x}\right)^2 + \left(\frac{\partial u}{\partial y}\right)^2 + \left(\frac{\partial v}{\partial x}\right)^2 + \left(\frac{\partial v}{\partial y}\right)^2 \right] + \rho_c A_v \left[\left(\frac{\partial u}{\partial z}\right)^2 + \left(\frac{\partial v}{\partial z}\right)^2 \right] , \tag{B2}$$

$$\varepsilon_{drag} = \rho_c C_d |\mathbf{U}|(Uu + Vv)|_{z=-H} \ , \tag{B3}$$

where ρ_c indicates the reference density, and A_h and A_v are horizontal and vertical eddy viscosity coefficients, respectively. (u, v) and (U, V) are horizontal baroclinic and total velocity, respectively. C_d is the bottom drag coefficient.

To calculate Eq. (B2), we need to know A_h. Although the variable is not an output field, we can obtain it through the information of the AE. According to Li et al. (2017), the average eddy viscosity in the SCS is 343 m^2 s^{-1}. Using their method, we estimate that in the AE on day 151, $A_h=436$ m^2 s^{-1}. The result is slightly larger than that in Li et al. (2017). For the convenience of calculation, we round off the horizontal eddy viscosity to $A_h=400$ m^2 s^{-1}.
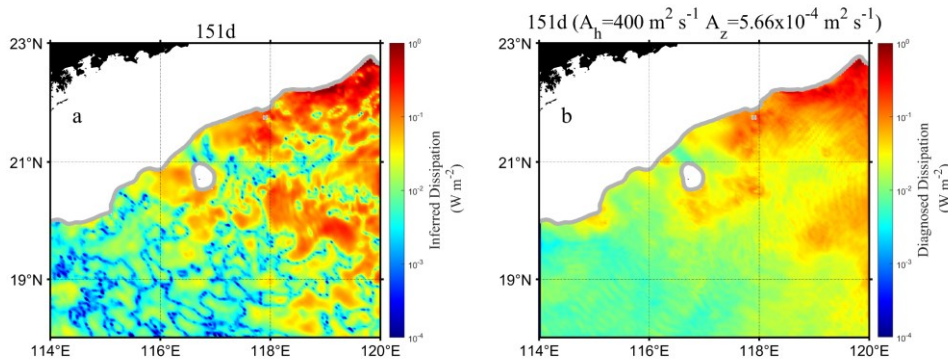
Figure B1. Inferred dissipation for the first five modes **(a)** and diagnosed dissipation **(b)** on day 151.

Figure B1a is the inferred result of $\sum_{n=1}^{5} \langle D_n \rangle$ according to Eq. (1), and Fig. B1b is the diagnosed result of Eq. (B1). In terms of magnitude, they both have energy dissipation rates that reach or exceed 10^{-1} W m^{-2} in the northeastern SCS. Their overall spatial patterns are similar, demonstrating that the energy equation of IT may achieve a better balance when considering the dissipation term. However, there are differences between Fig. B1a and Fig. B1b in some regions (such as near 118° E, 20° N),

which may be due to the fact that Fig. B1b uses the constant A_h, which is actually determined by the parameterization scheme in LLC4320, and the asymmetry of the eddy field may lead to spatial variations in A_h (Hu et al., 2011; Chen et al., 2012; Xu et al., 2016).

525

Appendix C

We decompose the incident and reflected energy fluxes of mode-1 and mode-3 SITs (Fig. C1 and Fig. C2). Figure C1 and Fig. C2 share a similar pattern for mode 1 and mode 3, indicating that energy reflection occurs when the incident SITs encounter the continental slope, which confirms that topographic reflection exists in different modes. The reflection of mode 1 influenced by the AE on day 151 is slightly smaller than that without eddy influence on day 137, implying that mesoscale eddy contributes to the reduced reflection of mode 1 SIT. Meanwhile, this suggests that the energy of mode-1 SIT is partially involved in the generation of the higher-mode SITs.
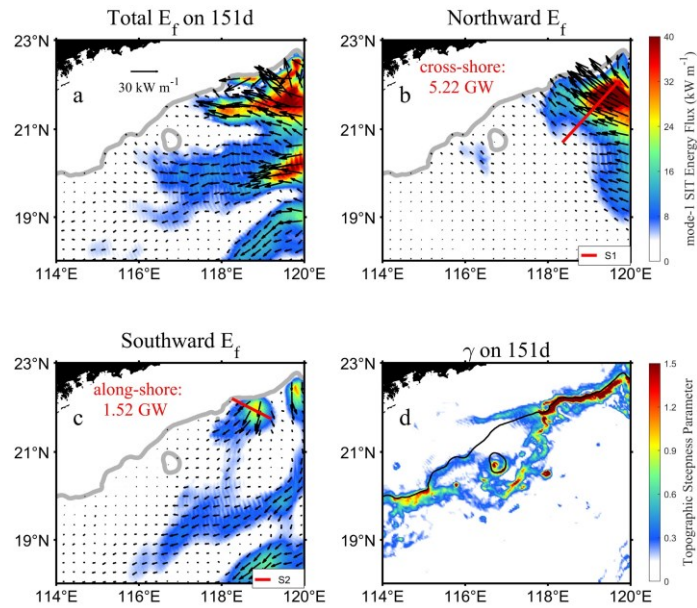
Figure C1. The energy flux of mode-1 SIT on day 151 in **(a)**, **(b)**, and **(c)** for total, northward, and southward, respectively. The energy fluxes integrated along sections S1 and S2 are labelled as cross-shore and along-shore values, respectively. The topographic steepness parameter for SIT on day 151 is presented in **(d)**.
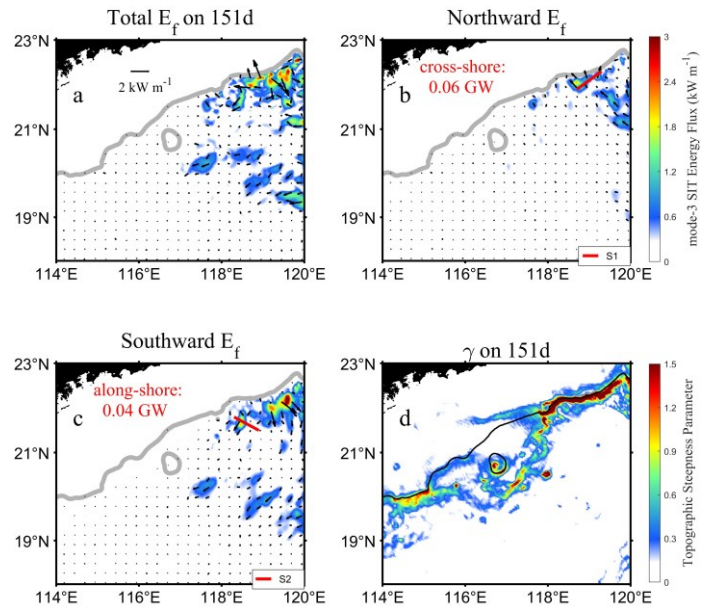
Figure C2. Same as Fig. C1, but for the mode 3.

540   *Data availability.* The MITgcm LLC4320 output is available at https://data.nas.nasa.gov/ecco/data.php, which was provided by Estimating the Circulation and Climate of the Oceans (ECCO) project and supported by High-End Computing (HEC) from the NASA Advanced Superconducting Division at the Ames Research Center. The TPXO-v9 data were obtained from https://www.tpxo.net/global/tpxo9-atlas, provided by Dr. Erofeeva from Oregon State University.

Author contributions. The study was conceived and designed by all co-authors. Data preparation, material collection, and
545   analysis were performed by LF. LF prepared the manuscript with contributions from all co-authors.

Acknowledgments. We are very grateful to Samuel M. Kelly for the discussions on the energy equation of internal tide. This work is jointly supported by the National Natural Science Foundation of China (grant 42076012, 42376012, 42006012).

Financial support. This research has been supported by the National Natural Science Foundation of China (grant no. 42076012, 42376012, 42006012).

550   References

Alford, M. H., MacKinnon, J. A., Nash, J. D., Simmons, H., Pickering, A., Klymak, J. M., Pinkel, R., Sun, O., Rainville, L., Musgrave, R., Beitzel, T., Fu, K., and Lu, C. W.: Energy flux and dissipation in Luzon Strait: Two tales of two ridges, J. Phys. Oceanogr., 41, 2211-2222, https://doi.org/10.1175/JPO-D-11-073.1, 2011.

Alford, M. H., Simmons, H. L., Marques, O. B., and Girton, J. B.: Internal tide attenuation in the North Pacific, Geophys. Res.
555   Lett., 46, 8205-8213, https://doi.org/10.1029/2019GL082648, 2019.

Alford, M. H., and Zhao, Z.: Global patterns of low-mode internal-wave propagation. Part II: Group velocity, J. Phys. Oceanogr., 37, 1849-1858, https://doi.org/10.1175/JPO3086.1, 2007.

Barkan, R., Srinivasan, K., Yang, L., McWilliams, J. C., Gula, J., and Vic, C.: Oceanic mesoscale eddy depletion catalyzed by internal waves, Geophys. Res. Lett., 48, e2021GL094376, https://doi.org/10.1029/2021GL094376, 2021.

560   Barkan, R., Winters, K. B., and McWilliams, J. C.: Stimulated imbalance and the enhancement of eddy kinetic energy dissipation by internal waves, J. Phys. Oceanogr., 47, 181-198, https://doi.org/10.1175/JPO-D-16-0117.1, 2017.

Book, D. L., Boris, J. P., and Hain, K.: Flux-corrected transport II: Generalizations of the method, J. Comput. Phys., 18, 248-283, https://doi.org/10.1016/0021-9991(75)90002-9, 1975.

Buijsman, M. C., Klymak, J. M., Legg, S., Alford, M. H., Farmer, D., MacKinnon, J. A., Nash, J. D., Park, J., Pickering, A.,
565   and Simmons, H.: Three-dimensional double-ridge internal tide resonance in Luzon Strait, J. Phys. Oceanogr., 44, 850-869, https://doi.org/10.1175/JPO-D-13-024.1, 2014.

Buijsman, M. C., Legg, S., and Klymak, J.: Double-ridge internal tide interference and its effect on dissipation in Luzon Strait, J. Phys. Oceanogr., 42, 1337-1356, https://doi.org/10.1175/JPO-D-11-0210.1, 2012.

Buijsman, M. C., Stephenson, G. R., Ansong, J. K., Arbic, B. K., Green, J. M., Richman, J. G., Shriver, J. F., Vic, C., Wallcraft., A. J., and Zhao, Z.: On the interplay between horizontal resolution and wave drag and their effect on tidal baroclinic mode waves in realistic global ocean simulations, Ocean Model., 152, 101656, https://doi.org/10.1016/j.ocemod.2020.101656, 2020.

Cao, A., Guo, Z., Lv, X., Song, J., and Zhang, J.: Coherent and incoherent features, seasonal behaviors, and spatial variations of internal tides in the northern South China Sea, J. Marine Syst., 172, 75-83, https://doi.org/10.1016/j.jmarsys.2017.03.005, 2017.

Chelton, D. B., Schlax, M. G., and Samelson, R. M.: Global observations of nonlinear mesoscale eddies, Prog. Oceanogr., 91, 167-216, https://doi.org/10.1016/j.pocean.2011.01.002, 2011.

Chen, G., Gan, J., Xie, Q., Chu, X., Wang, D., and Hou, Y.: Eddy heat and salt transports in the South China Sea and their seasonal modulations, J. Geophys. Res.-Ocean., 117, C05021, https://doi.org/10.1029/2011JC007724, 2012.

Chen, G., Hou, Y., and Chu, X.: Mesoscale eddies in the South China Sea: Mean properties, spatiotemporal variability, and impact on thermohaline structure, J. Geophys. Res.-Ocean., 116, C06018, https://doi.org/10.1029/2010JC006716, 2011.

Cheng, X., and Qi, Y.: Variations of eddy kinetic energy in the South China Sea, J. Oceanogr., 66, 85-94, https://doi.org/10.1007/s10872-010-0007-y, 2010.

Chu, X., Xue, H., Qi, Y., Chen, G., Mao, Q., Wang, D., and Chai, F.: An exceptional anticyclonic eddy in the South China Sea in 2010. J. Geophys. Res.-Ocean., 119, 881-897, h, 2014.

Clément, L., Frajka-Williams, E., Sheen, K. L., Brearley, J. A., and Garabato, A. N.: Generation of internal waves by eddies impinging on the western boundary of the North Atlantic, J. Phys. Oceanogr., 46, 1067-1079, https://doi.org/10.1175/JPO-D-14-0241.1, 2016.

Cummings, J. A., and Smedstad, O. M.: Variational data assimilation for the global ocean, in: Data Assimilation for Atmospheric, Oceanic and Hydrologic Applications, Vol. II, edited by: Park, S. K., and Xu, L., Springer, Berlin, Heidelberg, Germany, 303-343, https://doi.org/10.1007/978-3-642-35088-7, 2013.

Cusack, J. M., Brearley, J. A., Garabato, A. C. N., Smeed, D. A., Polzin, K. L., Velzeboer, N., and Shakespeare, C. J.: Observed eddy–internal wave interactions in the Southern Ocean, J. Phys. Oceanogr., 50, 3043-3062, https://doi.org/10.1175/JPO-D-20-0001.1, 2020.

Da Silva, J. C. B., New, A. L., Srokosz, M. A., and Smyth, T. J.: On the observability of internal tidal waves in remotely-sensed ocean colour data, Geophys. Res. Lett., 29, 10-14, https://doi.org/10.1029/2001GL013888, 2002.

Duda, T. F., Lin, Y. T., Newhall, A. E., Helfrich, K. R., Zhang, W. G., Badiey, M., Lermusiaux, P. F., Colosi, J. A., and Lynch, J. F.: The 'Integrated Ocean Dynamics and Acoustics'(IODA) hybrid modeling effort, in: Proceedings of the international conference on Underwater Acoustics-2014, Rhodes, Greece, 22-27 June 2014, 621-628, 2014.

600   Dunphy, M., and Lamb, K. G.: Focusing and vertical mode scattering of the first mode internal tide by mesoscale eddy interaction, J. Geophys. Res.-Ocean., 119, 523-536, https://doi.org/10.1002/2013JC009293, 2014.

Dunphy, M., Ponte, A. L., Klein, P., and Le Gentil, S.: Low-mode internal tide propagation in a turbulent eddy field, J. Phys. Oceanogr., 47, 649-665, https://doi.org/10.1175/JPO-D-16-0099.1, 2017.

Egbert, G. D., Erofeeva, S. Y., Egbert, G. D. and Erofeeva, S. Y.: Efficient inverse modeling of barotropic ocean tides, J.
605   Atmos. Ocean. Tech., 19, 183-204, https://doi.org/10.1175/1520-0426(2002)019<0183:EIMOBO>2.0.CO;2, 2002.

Egbert, G. D., and Ray, R. D.: Semi-diurnal and diurnal tidal dissipation from TOPEX/Poseidon altimetry, Geophys. Res. Lett., 30, 1907, https://doi.org/10.1029/2003GL017676, 2003.

Faghmous, J. H., Frenger, I., Yao, Y., Warmka, R., Lindell, A., and Kumar, V.: A daily global mesoscale ocean eddy dataset from satellite altimetry, Sci. Data, 2, 1-16, https://doi.org/10.1038/sdata.2015.28, 2015.

610   Fernández-Castro, B., Evans, D. G., Frajka-Williams, E., Vic, C., and Naveira-Garabato, A. C.: Breaking of internal waves and turbulent dissipation in an anticyclonic mode water eddy, J. Phys. Oceanogr., 50, 1893-1914, https://doi.org/10.1175/JPO-D-19-0168.1, 2020.

Ferrari, R., and Wunsch, C.: Ocean circulation kinetic energy: Reservoirs, sources, and sinks, Annu. Rev. Fluid Mech., 41, 253-282, https://doi.org/10.1146/annurev.fluid.40.111406.102139, 2009.

615   Goldsworth, F., Marshall, D., and Johnson, H.: Symmetric instability in cross-equatorial western boundary currents, J. Phys. Oceanogr., 51, 2049-2067, https://doi.org/10.1175/JPO-D-20-0273.1, 2021.

Gong, Y., Rayson, M. D., Jones, N. L., and Ivey, G. N.: Directional decomposition of internal tides propagating from multiple generation sites, Ocean Model., 162, 101801, https://doi.org/10.1016/j.ocemod.2021.101801, 2021.

Guo, P., Fang, W., Liu, C., and Qiu, F.: Seasonal characteristics of internal tides on the continental shelf in the northern South
620   China Sea, J. Geophys. Res.-Ocean., 117, C04023, https://doi.org/10.1029/2011JC007215, 2012.

Guo, Z., Wang, S., Cao, A., Xie, J., Song, J., and Guo, X.: Refraction of the M_2 internal tides by mesoscale eddies in the South China Sea, Deep-Sea Res. Pt. I, 192, 103946, https://doi.org/10.1016/j.dsr.2022.103946, 2023.

Hamann, M. M., Alford, M. H., Lucas, A. J., Waterhouse, A. F., and Voet, G.: Turbulence driven by reflected internal tides in a supercritical submarine canyon, J. Phys. Oceanogr., 51, 591-609, https://doi.org/10.1175/JPO-D-20-0123.1, 2021.

625   Hu, J., Gan, J., Sun, Z., Zhu, J., and Dai, M.: Observed three-dimensional structure of a cold eddy in the southwestern South China Sea, J. Geophys. Res.-Ocean., 116, C05016, https://doi.org/10.1029/2010JC006810, 2011.

Hu, Q., Huang, X., Zhang, Z., Zhang, X., Xu, X., Sun, H., Zhou, C., Zhao, W., and Tian, J.: Cascade of internal wave energy catalyzed by eddy-topography interactions in the deep South China Sea, Geophys. Res. Lett., 47, e2019GL086510, https://doi.org/10.1029/2019GL086510, 2020.

630   Huang, X., Wang, Z., Zhang, Z., Yang, Y., Zhou, C., Yang, Q., Zhao, W., and Tian, J.: Role of mesoscale eddies in modulating the semidiurnal internal tide: Observation results in the northern South China Sea, J. Phys. Oceanogr., 48, 1749-1770, https://doi.org/10.1175/JPO-D-17-0209.1, 2018.

Jan, S., Lien, R. C., and Ting, C. H.: Numerical study of baroclinic tides in Luzon Strait, J. Oceanogr., 64, 789-802, https://doi.org/10.1007/s10872-008-0066-5, 2008.

635 Kang, D., and Fringer, O.: Energetics of barotropic and baroclinic tides in the Monterey Bay area, J. Phys. Oceanogr., 42, 272-290, https://doi.org/10.1175/JPO-D-11-039.1, 2012.

Kelly, S. M., and Lermusiaux, P. F.: Internal-tide interactions with the Gulf Stream and Middle Atlantic Bight shelfbreak front, J. Geophys. Res.-Ocean., 121, 6271-6294, https://doi.org/10.1002/2016JC011639, 2016a.

Kelly, S. M., Lermusiaux, P. F., Duda, T. F., and Haley Jr, P. J.: A coupled-mode shallow-water model for tidal analysis:
640 Internal tide reflection and refraction by the Gulf Stream, J. Phys. Oceanogr., 46, 3661-3679, https://doi.org/ 10.1175/JPO-D-16-0018.1, 2016b.

Kelly, S. M., Nash, J. D., Martini, K. I., Alford, M. H., and Kunze, E.: The cascade of tidal energy from low to high modes on a continental slope, J. Phys. Oceanogr., 42, 1217-1232, https://doi.org/10.1175/JPO-D-11-0231.1, 2012.

Kelly, S. M., Jones, N. L., and Nash, J. D.: A coupled model for Laplace's tidal equations in a fluid with one horizontal
645 dimension and variable depth, J. Phys. Oceanogr., 43, 1780-1797, https://doi.org/10.1175/JPO-D-12-0147.1, 2013.

Kelly, S. M., Waterhouse, A. F., and Savage, A. C.: Global dynamics of the stationary M_2 mode-1 internal tide, Geophys. Res. Lett., 48, e2020GL091692, https://doi.org/10.1029/2020GL091692, 2021.

Kerry, C. G., Powell, B. S., and Carter, G. S. Effects of remote generation sites on model estimates of M_2 internal tides in the Philippine Sea. J. Phys. Oceanogr., 43, 187-204, https://doi.org/10.1175/JPO-D-12-081.1, 2013.

650 Krauss, W.: Internal tides resulting from the passage of surface tides through an eddy field, J. Geophys. Res.-Ocean., 104, 18323-18331, https://doi.org/10.1029/1999JC900067, 1999.

Kvale, E. P.: The origin of neap-spring tidal cycles, Mar. Geol., 235, 5-18, https://doi.org/10.1016/j.margeo.2006.10.001, 2006.

Lahaye, N., Gula, J., and Roullet, G.: Internal tide cycle and topographic scattering over the North Mid-Atlantic Ridge, J. Geophys. Res.-Ocean., 125, e2020JC016376, https://doi.org/10.1029/2020JC016376, 2020.

655 Legg, S.: Scattering of low-mode internal waves at finite isolated topography, J. Phys. Oceanogr., 44, 359-383, https://doi.org/10.1175/JPO-D-12-0241.1, 2014.

Lelong, M. P., and Kunze, E.: Can barotropic tide–eddy interactions excite internal waves?, J. Fluid Mech., 721, 1-27, https://doi.org/10.1017/jfm.2013.1, 2013.

Lermusiaux, P. F., Xu, J., Chen, C. F., Jan, S., Chiu, L. Y., and Yang, Y. J.: Coupled ocean–acoustic prediction of transmission
660 loss in a continental shelfbreak region: Predictive skill, uncertainty quantification, and dynamical sensitivities, IEEE J. Oceanic Eng., 35, 895-916, https://doi.org/10.1109/JOE.2010.2068611, 2010.

Li, M., Hou, Y., Li, Y., and Hu, P.: Energetics and temporal variability of internal tides in Luzon Strait: a nonhydrostatic numerical simulation, Chin. J. Oceanol. Limn., 30, 852-867, https://doi.org/10.1007/s00343-012-1289-2, 2012.

Li, Q.: Numerical assessment of factors affecting nonlinear internal waves in the South China Sea, Prog. Oceanogr., 121, 24-
665 43, https://doi.org/10.1016/j.pocean.2013.03.006, 2014.

Li, Q., Sun, L., and Xu, C.: The lateral eddy viscosity derived from the decay of oceanic mesoscale eddies, Open J. Mar. Sci., 8, 152-172, https://doi.org/10.4236/ojms.2018.81008, 2017.

Lin, H., Liu, Z., Hu, J., Menemenlis, D., and Huang, Y.: Characterizing meso-to submesoscale features in the South China Sea, Prog. Oceanogr., 188, 102420, https://doi.org/10.1016/j.pocean.2020.102420, 2020.

670 Lin, X., Dong, C., Chen, D., Liu, Y., Yang, J., Zou, B., and Guan, Y.: Three-dimensional properties of mesoscale eddies in the South China Sea based on eddy-resolving model output, Deep Sea Res. Pt. I, 99, 46-64, https://doi.org/10.1016/j.dsr.2015.01.007, 2015.

Liu, J., He, Y., Wang, D., Liu, T., and Cai, S.: Observed enhanced internal tides in winter near the Luzon Strait, J. Geophys. Res.-Ocean., 120, 6637-6652, https://doi.org/10.1002/2015JC011131, 2015.

675 Liu, M., Chen, R., Flierl, G. R., Guan, W., Zhang, H., and Geng, Q.: Scale-dependent eddy diffusivities at the Kuroshio Extension: A particle-based estimate and comparison to theory, J. Phys. Oceanogr., In press, https://doi.org/10.1175/JPO-D-22-0223.1, 2023.

Liu, Q., Xie, X., Shang, X., Chen, G., and Wang, H.: Modal structure and propagation of internal tides in the northeastern South China Sea, Acta. Oceanol. Sin., 38, 12-23, https://doi.org/10.1007/s13131-019-1473-1, 2019.

680 Liu, Y., Zhang, X., Sun, Z., Zhang, Z., Sasaki, H., Zhao, W., and Tian, J.: Region-dependent eddy kinetic energy budget in the northeastern South China Sea revealed by submesoscale-permitting simulations. J. Marine Syst., 235, 103797, https://doi.org/10.1016/j.jmarsys.2022.103797, 2022.

Liu, Z., and Gan, J.: Open boundary conditions for tidally and subtidally forced circulation in a limited-area coastal model using the Regional ing System (ROMS), J. Geophys. Res.-Ocean., 121, 6184-6203, https://doi.org/10.1002/2016JC011975,
685 2016.

Löb, J., Köhler, J., Mertens, C., Walter, M., Li, Z., von Storch, J. S., Zhao, Z., and Rhein, M.: Observations of the low-mode internal tide and its interaction with mesoscale flow south of the Azores, J. Geophys. Res.-Ocean., 125, e2019JC015879, https://doi.org/10.1029/2019JC015879, 2020.

Marshall, J., Adcroft, A., Hill, C., Perelman, L., and Heisey, C.: A finite-volume, incompressible Navier Stokes model for
690 studies of the ocean on parallel computers, J. Geophys. Res.-Ocean., 102, 5753-5766, https://doi.org/10.1029/96JC02775, 1997.

Martini, K. I., Alford, M. H., Nash, J. D., Kunze, E., and Merrifield, M. A.: Diagnosing a partly standing internal wave in Mamala Bay, Oahu, Geophys. Res. Lett., 34, L17604, https://doi.org/10.1029/2007GL029749, 2007.

Mazloff, M. R., Cornuelle, B., Gille, S. T., and Wang, J.: The importance of remote forcing for regional modeling of internal
695 waves, J. Geophys. Res.-Ocean., 125, e2019JC015623, https://doi.org/10.1029/2019JC015623, 2020.

McGillicuddy Jr, D. J., Anderson, L. A., Bates, N. R., Bibby, T., Buesseler, K. O., Carlson, C. A., Davis, C. S., Ewart, C., Falkowski, P. G., Goldthwait, S. A. Hansell, D. A., Jenkins, W. J., Johnson, R., Kosnyrev, V. K., Ledwell, J. R., Li, Q. P., Siegel, D. A., and Steinberg, D. K.: Eddy/wind interactions stimulate extraordinary mid-ocean plankton blooms, Science, 316, 1021-1026, https://doi.org/10.1126/science.1136256, 2007.

700 Menemenlis, D., Hill, C., Henze, C. E., Wang, J., and Fenty, I.: Pre-SWOT Level-4 Hourly MITgcm LLC4320 Native 2km Grid Oceanographic Version 1.0, https ://doi.org/10.5067/PRESW-YOJ10, 2021.

Müller, M., Cherniawsky, J. Y., Foreman, M. G. G., and von Storch, J. S.: Global M_2 internal tide and its seasonal variability from high resolution ocean circulation and tide modelling, Geophys. Res. Lett., 39, L19607, https://doi.org/10.1029/2012GL053320, 2012.

705 Munk, W., and Wunsch, C.: Abyssal recipes II: Energetics of tidal and wind mixing, Deep Sea Res. Pt. I, 45, 1977-2010, https://doi.org/10.1016/S0967-0637(98)00070-3, 1998.

Nikurashin, M., and Legg, S.: A mechanism for local dissipation of internal tides generated at rough topography, J. Phys. Oceanogr., 41, 378-395, https://doi.org/10.1175/2010JPO4522.1, 2011.

Niwa, Y., and Hibiya, T.: Three-dimensional numerical simulation of M_2 internal tides in the East China Sea, J. Geophys.
710 Res.-Ocean., 109, C04027, https://doi.org/10.1029/2003JC001923, 2004.

Pan, Y., Haley, P. J., and Lermusiaux, P. F.: Interactions of internal tides with a heterogeneous and rotational ocean, J. Fluid Mech., 920, A18, https://doi.org/ 10.1017/jfm.2021.423, 2021.

Park, J. H., and Farmer, D.: Effects of Kuroshio intrusions on nonlinear internal waves in the South China Sea during winter, J. Geophys. Res.-Ocean., 118, 7081-7094, https://doi.org/10.1002/2013JC008983, 2013.

715 Pedlosky, J.: Waves in the ocean and atmosphere: introduction to wave dynamics, Vol. 260, Springer, Berlin, Germany, https://doi.org/10.1007/978-3-662-05131-3, 2003.

Polzin, K. L.: Mesoscale eddy–internal wave coupling. Part II: Energetics and results from PolyMode, J. Phys. Oceanogr., 40, 789-801, https://doi.org/10.1175/2009JPO4039.1, 2010.

Rocha, C. B., Chereskin, T. K., Gille, S. T., and Menemenlis, D.: Mesoscale to submesoscale wavenumber spectra in Drake
720 Passage, J. Phys. Oceanogr., 46, 601-620, https://doi.org/10.1175/JPO-D-15-0087.1, 2016.

Savage, A. C., Waterhouse, A. F., and Kelly, S. M.: Internal tide nonstationarity and wave–mesoscale interactions in the Tasman Sea, J. Phys. Oceanogr., 50, 2931-2951, https://doi.org/10.1175/JPO-D-19-0283.1, 2020.

Sharples, J., Moore, C. M., Hickman, A. E., Holligan, P. M., Tweddle, J. F., Palmer, M. R., and Simpson, J. H.: Internal tidal mixing as a control on continental margin ecosystems, Geophys. Res. Lett., 36, L23603,
725 https://doi.org/10.1029/2009GL040683, 2009.

Smyth, W. D., Moum, J. N., and Nash, J. D.: Narrowband oscillations in the upper equatorial ocean. Part II: Properties of shear instabilities, J. Phys. Oceanogr., 41, 412-428, https://doi.org/10.1175/2010JPO4451.1, 2011.

Stastna, M., and Lamb, K. G.: Sediment resuspension mechanisms associated with internal waves in coastal waters, J. Geophys. Res.-Ocean., 113, C10016, https://doi.org/10.1029/2007JC004711, 2008.

730 St. Laurent, L., and Garrett, C.: The role of internal tides in mixing the deep ocean, J. Phys. Oceanogr., 32, 2882-2899, https://doi.org/10.1175/1520-0485(2002)032<2882:TROITI>2.0.CO;2, 2002.

Su, Z., Torres, H., Klein, P., Thompson, A. F., Siegelman, L., Wang, J., Menemenlis, D., and Hill, C.: High-frequency submesoscale motions enhance the upward vertical heat transport in the global ocean, J. Geophys. Res.-Ocean., 125, e2020JC016544, https://doi.org/10.1029/2020JC016544, 2020.

Tian, J., Yang, Q., and Zhao, W.: Enhanced diapycnal mixing in the South China Sea, J. Phys. Oceanogr., 39, 3191-3203, https://doi.org/10.1175/2009JPO3899.1, 2009.

Vic, C., Naveira Garabato, A. C., Green, J. M., Waterhouse, A. F., Zhao, Z., Melet, A., de Lavergne, C., Buijsman, M. C., and Stephenson, G. R.: Deep-ocean mixing driven by small-scale internal tides, Nat. commun., 10, 2099, https://doi.org/10.1038/s41467-019-10149-5, 2019.

Wang, S., Cao, A., Li, Q., and Chen, X.: Reflection of K_1 internal tides at the continental slope in the northern South China Sea, J. Geophys. Res.-Ocean., 126, e2021JC017260, https://doi.org/10.1029/2021JC017260, 2021.

Wang, X., Peng, S., Liu, Z., Huang, R. X., Qian, Y. K., and Li, Y.: Tidal mixing in the South China Sea: An estimate based on the internal tide energetics, J. Phys. Oceanogr., 46, 107-124, https://doi.org/10.1175/JPO-D-15-0082.1, 2016.

Wang, Y., and Legg, S.: Enhanced Dissipation of Internal Tides in a Mesoscale Baroclinic Eddy. J. Phys. Oceanogr., 53, 2293-2316, https://doi.org/10.1175/JPO-D-23-0045.1, 2023.

Wang, Y., Xu, Z., Hibiya, T., Yin, B., and Wang, F.: Radiation path of diurnal internal tides in the Northwestern pacific controlled by refraction and interference, J. Geophys. Res.-Ocean., 126, e2020JC016972, https://doi.org/10.1029/2020JC016972, 2021.

Whalen, C. B., MacKinnon, J. A., and Talley, L. D.: Large-scale impacts of the mesoscale environment on mixing from wind-driven internal waves, Nat. Geosic., 11, 842-847, https://doi.org/10.1038/s41561-018-0213-6, 2018.

Wu, L., Miao, C., and Zhao, W.: Patterns of K_1 and M_2 internal tides and their seasonal variations in the northern South China Sea, J. Oceanogr., 69, 481-494, https://doi.org/10.1007/s10872-013-0183-7, 2013.

Wunsch, C.: Where do ocean eddy heat fluxes matter?, J. Geophys. Res.-Ocean., 104, 13235-13249, https://doi.org/10.1029/1999JC900062, 1999.

Xu, L., Li, P., Xie, S. P., Liu, Q., Liu, C., and Gao, W.: Observing mesoscale eddy effects on mode-water subduction and transport in the North Pacific, Nat. commun., 7, 10505, https://doi.org/10.1038/ncomms10505, 2016.

Xu, Z., Liu, K., Yin, B., Zhao, Z., Wang, Y., and Li, Q.: Long-range propagation and associated variability of internal tides in the South China Sea, J. Geophys. Res.-Ocean., 121, 8268-8286, https://doi.org/10.1002/2016JC012105, 2016.

Xu, Z., Wang, Y., Liu, Z., McWilliams, J. C., and Gan, J.: Insight into the dynamics of the radiating internal tide associated with the Kuroshio Current. J. Geophys. Res.-Ocean., 126, e2020JC017018, https://doi.org/10.1029/2020JC017018, 2021.

Yang, Q., Nikurashin, M., Sasaki, H., Sun, H., and Tian, J.: Dissipation of mesoscale eddies and its contribution to mixing in the northern South China Sea, Sci. Rep. -UK, 9, 556, https://doi.org/10.1038/s41598-018-36610-x, 2019.

Yang, Q., Zhao, W., Liang, X., and Tian, J.: Three-dimensional distribution of turbulent mixing in the South China Sea, J. Phys. Oceanogr., 46, 769-788, https://doi.org/10.1175/JPO-D-14-0220.1, 2016.

765 You, J., Xu, Z., Li, Q., Robertson, R., Zhang, P., and Yin, B.: Enhanced internal tidal mixing in the Philippine Sea mesoscale environment, Nonlinear Proc. Geoph., 28, 271-284, https://doi.org/10.5194/npg-28-271-2021, 2021.

You, J., Xu, Z., Li, Q., Zhang, P., Yin, B., and Hou, Y.: M_2 Internal Tide Energetics and Behaviors in the Subpolar North Pacific, J. Phys. Oceanogr., 53, 1269-1290, https://doi.org/10.1175/JPO-D-22-0032.1, 2023.

You, J., Xu, Z., Zhang, P., Hu, X., Liao, G., Yin, B., and Robertson, R.: Mixing in the Philippine Sea: Geography variability
770   and parameterization, Deep-Sea Res. Pt. II: Topical Studies in Oceanography, 202, 105143, https://doi.org/10.1016/j.dsr2.2022.105143, 2022.

Yu, X., Ponte, A. L., Elipot, S., Menemenlis, D., Zaron, E. D., and Abernathey, R.: Surface kinetic energy distributions in the global oceans from a high-resolution numerical model and surface drifter observations, Geophys. Res. Lett., 46, 9757-9766, https://doi.org/10.1029/2019GL083074, 2019.

775 Zaron, E. D., and Egbert, G. D.: Time-variable refraction of the internal tide at the Hawaiian Ridge, J. Phys. Oceanogr., 44, 538-557, https://doi.org/10.1175/JPO-D-12-0238.1, 2014.

Zaron, E. D., Musgrave, R. C., and Egbert, G. D.: Baroclinic tidal energetics inferred from satellite altimetry, J. Phys. Oceanogr., 52, 1015-1032, https://doi.org/10.1175/JPO-D-21-0096.1, 2022.

Zhang, Z., Liu, Y., Qiu, B., Luo, Y., Cai, W., Yuan, Q., Liu, Y., Zhang, H., Liu, H., Miao, M., Zhao, J., Zhao, W., and Tian,
780   J.: Submesoscale inverse energy cascade enhances Southern Ocean eddy heat transport, Nat. commun., 14, 1335, https://doi.org/10.1038/s41467-023-36991-2, 2023.

Zhang, Z., Tian, J., Qiu, B., Zhao, W., Chang, P., Wu, D., and Wan, X.: Observed 3D structure, generation, and dissipation of oceanic mesoscale eddies in the South China Sea, Sci. Rep. -UK, 6, 24349, https://doi.org/10.1038/srep24349, 2016.

Zhang, Z., Wang, W., and Qiu, B.: Oceanic mass transport by mesoscale eddies, Science, 345, 322-324,
785   https://doi.org/10.1126/science.1252418, 2014.

Zhao, Z.: The global mode-1 S_2 internal tide, J. Geophys. Res.-Ocean., 122, 8794-8812, https://doi.org/10.1002/2017JC013112, 2017.

Zhao, Z., Alford, M. H., Girton, J. B., Rainville, L., and Simmons, H. L.: Global observations of open-ocean mode-1 M_2 internal tides, J. Phys. Oceanogr., 46, 1657-1684, https://doi.org/10.1175/JPO-D-15-0105.1, 2016.

790 Zhao, Z., Alford, M. H., MacKinnon, J. A., and Pinkel, R.: Long-range propagation of the semidiurnal internal tide from the Hawaiian Ridge, J. Phys. Oceanogr., 40, 713-736, https://doi.org/10.1175/2009JPO4207.1, 2010.

Zhao, Z., and Qiu, B.: Seasonal west-east seesaw of M_2 internal tides from the Luzon Strait, J. Geophys. Res.-Ocean., e2022JC019281, https://doi.org/10.1029/2022JC019281, 2023.

Zhou, C., Xiao, X., Zhao, W., Yang, J., Huang, X., Guan, S., Zhang, Z., and Tian, J.: Increasing deep-water overflow from the
795   Pacific into the South China Sea revealed by mooring observations, Nat. commun., 14, 2013, https://doi.org/10.1038/s41467-023-37767-4, 2023.